ORIGINAL ARTICLE

Vibration Control of the Rail Grinding Vehicle with Abrasive Belt Based on Structural Optimization and Lightweight Design

Wengang Fan[1,2]* , Shuai Zhang[1,2], Zhiwei Wu[1,2], Yi Liu[1,2] and Jiangnan Yu[3]

Abstract

As a new grinding and maintenance technology, rail belt grinding shows significant advantages in many applications. The dynamic characteristics of the rail belt grinding vehicle largely determines its grinding performance and service life. In order to explore the vibration control method of the rail grinding vehicle with abrasive belt, the vibration response changes in structural optimization and lightweight design are respectively analyzed through transient response and random vibration simulations in this paper. Firstly, the transient response simulation analysis of the rail grinding vehicle with abrasive belt is carried out under operating conditions and non-operating conditions. Secondly, the vibration control of the grinding vehicle is implemented by setting vibration isolation elements, optimizing the structure, and increasing damping. Thirdly, in order to further explore the dynamic characteristics of the rail grinding vehicle, the random vibration simulation analysis of the grinding vehicle is carried out under the condition of the horizontal irregularity of the American AAR6 track. Finally, by replacing the Q235 steel frame material with 7075 aluminum alloy and LA43M magnesium alloy, both vibration control and lightweight design can be achieved simultaneously. The results of transient dynamic response analysis show that the acceleration of most positions in the two working conditions exceeds the standard value in GB/T 17426-1998 standard. By optimizing the structure of the grinding vehicle in three ways, the average vibration acceleration of the whole car is reduced by about 55.1% from 15.6 m/s^2 to 7.0 m/s^2. The results of random vibration analysis show that the grinding vehicle with Q235 steel frame does not meet the safety conditions of 3σ. By changing frame material, the maximum vibration stress of the vehicle can be reduced from 240.7 MPa to 160.0 MPa and the weight of the grinding vehicle is reduced by about 21.7% from 1500 kg to 1175 kg. The modal analysis results indicate that the vibration control of the grinding vehicle can be realized by optimizing the structure and replacing the materials with lower stiffness under the premise of ensuring the overall strength. The study provides the basis for the development of lightweight, diversified and efficient rail grinding equipment.

Keywords Vibration control, Dynamic characteristics, Structural optimization, Lightweight design, Modal analysis

*Correspondence:
Wengang Fan
wgfan@bjtu.edu.cn
[1] School of Mechanical, Electronic and Control Engineering, Beijing Jiaotong University, Beijing 100044, China
[2] Key Laboratory of Vehicle Advanced Manufacturing, Measuring and Control Technology, Ministry of Education, Beijing 100044, China
[3] China Railway Materials Operation and Maintenance Technology Co., Ltd, Beijing 100036, China

1 Introduction

Rail grinding technology plays an important role in railway maintenance [1–3]. Due to the rapid development of China's railways, diverse efficient and intelligent rail grinding technologies and devices have been developed [4]. Rail grinding vehicles with abrasive belt have the advantages of lightweight, flexibility, integration, energy conservation, and environmental protection. However, the performance of grinding vehicles are affected by the

Fan *et al. Chinese Journal of Mechanical Engineering*   (2024) 37:68

Page 2 of 27

vibration caused by various excitations. Therefore, vibration control measures are significant in the development of diverse efficient rail grinding vehicles [5], such as structural optimization and lightweight design.

Dynamic simulation is widely applied in the field of railway vehicles [6]. The study on dynamic characteristics of railway vehicles involves both transient response and random vibration. Through dynamic simulation, the vibration characteristics of the vehicle system can be analyzed for its structural optimization [7]. Hillerborg et al. [8] established a multi-rigid vehicle model with only 2 degrees of freedom and connected to two mass blocks by a spring. In the model, for the convenience of the vibration analysis of wheelset, only the *Z*-direction vibration of the vehicle was considered. Vehicle dynamics have been explored in this way [9–11]. Yi et al. [12] established a dynamic analysis model of the deflection mechanism of a rail grinding vehicle with the finite element method and carried out the dynamic simulation analyses of the mechanism, including dynamic response analysis and modal analysis. The finite element method is widely applied in the field of rail grinding [13–17].

Two methods are mainly used to realize the vibration control of rail vehicles, namely, passive vibration reduction and active vibration reduction. Regarding passive vibration control, Zhang et al. [18] proposed a new vibration control method for building vibration suppression and vehicle suspension design, the structure-immittance method, and verified the method through simulation. Many scholars achieved passive vibration control by optimizing the structure and changing materials [19, 20]. Regarding active vibration control, İkbalEski et al. [21] used a robust artificial neural network to design a control system for the problem of vehicle vibration caused by road surface irregularities and confirmed that the control system performed better in the adaptation to the random road disturbance of vehicle suspension. Many scholars realized active vibration control through algorithms [22–26].

Lightweight design methods can be divided into structural optimization and material replacement. JANG et al. [27] developed a novel ultra-lightweight frame for a flatbed trailer, optimized the thicknesses of the member plates and the boundary shapes with the Taguchi method through computer aided engineering (CAE) software, improved frame bending and torsional stiffness, and reduced its mass by 24.5% compared to the original model. This structural optimization method is widely favored by many researchers in the lightweight design field [28–31]. However, the structure of the rail grinding vehicle determines its stability and grinding quality, thus leading to some limitations in optimizing the structure. Therefore, it is necessary to changing the frame material

for the lightweight design. Bletzinger et al. [31] indicated that the steel material of the vehicle could be replaced by aluminum, magnesium, and plastic. Alternatives to the steel unibody are multimaterial units and aluminum space frames. This method of changing materials is also widely adopted by many researchers [32–35].

The study on dynamic characteristics is important in vibration control for optimizing the grinding vehicle. However, relevant studies on a rail grinding vehicle with abrasive belt were seldom reported. In this study, with a rail grinding vehicle with abrasive belt as the research object, the modes of the entire vehicle and its components are analyzed. Next, the transient dynamics of the grinding vehicle are studied under operating conditions and non-operating conditions and passive vibration control is carried out by setting vibration isolation elements, optimizing the structure, and increasing damping ways. Then, the dynamic characteristics of the grinding vehicle are further studied by random vibration simulation under the power spectral density of the horizontal irregularity of the American AAR6 track and both the lightweight design and vibration control are simultaneously realized by replacing Q235 steel frame material with 7075 aluminum alloy and LA43M magnesium alloy.

2 Modal Analysis
Through modal analysis, the natural frequencies of the various parts can be obtained for subsequent dynamic analysis.

2.1 Finite Element Model and Excitation of the Grinding Vehicle
In the Hypermesh software, the motor and electrical devices are simulated by mass points and Reb3 units. The underframe and frame are formed by welding channel steel and aluminum alloy. The wheelset is composed of chrome bearing steel and carbon steel. The grinding unit is composed of aluminum alloy and rubber and the skin is an aluminum alloy plate. The length-thickness ratio of channel steel and aluminum alloy in the grinding vehicle is large, so the underframe, skin, and frame structure are simulated by shell elements with a size of 10 mm in order to reduce the calculation cost. The wheelset and grinding units are solid units with a size of 5 mm so as to increase model accuracy. Welding is simulated by the spot unit and the bolt and bearing connection are simulated by the rigid unit and beam unit. Each contact surface is initially in a contact state with a certain stiffness.

In the solution process in Nastran software, the simulated damping is viscous damping and structural damping. According to the previous report, the critical damping ratio of the structure is generally in the range of 0 to 10% [36]. Therefore, the critical damping percentage

is set to 3% and the overall structural damping coefficient is 6% [37]. In the dynamic response analysis, the structural damping is converted into equivalent viscous damping. The material properties of each component are shown in Table 1.

The finite element model of the rail grinding vehicle with abrasive belt is established in Hypermesh with a total of 3.23 million nodes and 2.76 million elements, as shown in Figure 1.

Figures 1(e), (f), (g), and (h) show the excitations received by the grinding vehicle under operating conditions. Figure 1(e) is the wheel out-of-round excitation. From November 2011 to May 2014, Yuan's research

group conducted a large number of tests on the wheel shape of a certain type of EMU wheel. In the test data obtained, the main components that make up the wheel are basically within the 20 order, of which the 1-6 order is relatively significant. In the wheels of the new wheel and the new repair, the wheel is not round and mainly has 1-3 order [36]. According to Yuan's research on wheel out-of-roundness and the design requirements of the explored grinding vehicle, the wheel out-of-roundness in this paper is a 1-3 order wheel polygon and the radial runout value is 0.04 mm. The belt-type rail grinding vehicle has a wheel diameter of 370 mm, a maximum travel speed of 20 km/h, and a maximum grinding speed of 10 km/h. The excitation frequency range of wheel out-of-roundness is 4.78 to 15 Hz under non-operating conditions and the excitation frequency range of wheel out-of-roundness under operating conditions is 3 to 9 Hz.

Figures 1(f) and (h) show the rail corrugation excitation, which belongs to the continuous harmonic displacement excitation. According to the calculation results of rail corrugation of Liu [38], the main grinding wavelength of rail grinding vehicle with abrasive belt is approximately 50 to 150 mm and the wave depth is approximately 0.1 mm. The excitation range of the track is 37.04 to 111.11

Table 1 Modeling material table of the finite element model

Materials	Density (g/cm³)	Elastic modulus (GPa)	Poisson's ratio
Steel Q235	7.85	210	0.30
Aluminum alloy 6061	2.70	70	0.33
Bearing steel GCr15	7.85	206	0.30
Rubber	1.02	0.00784	0.48
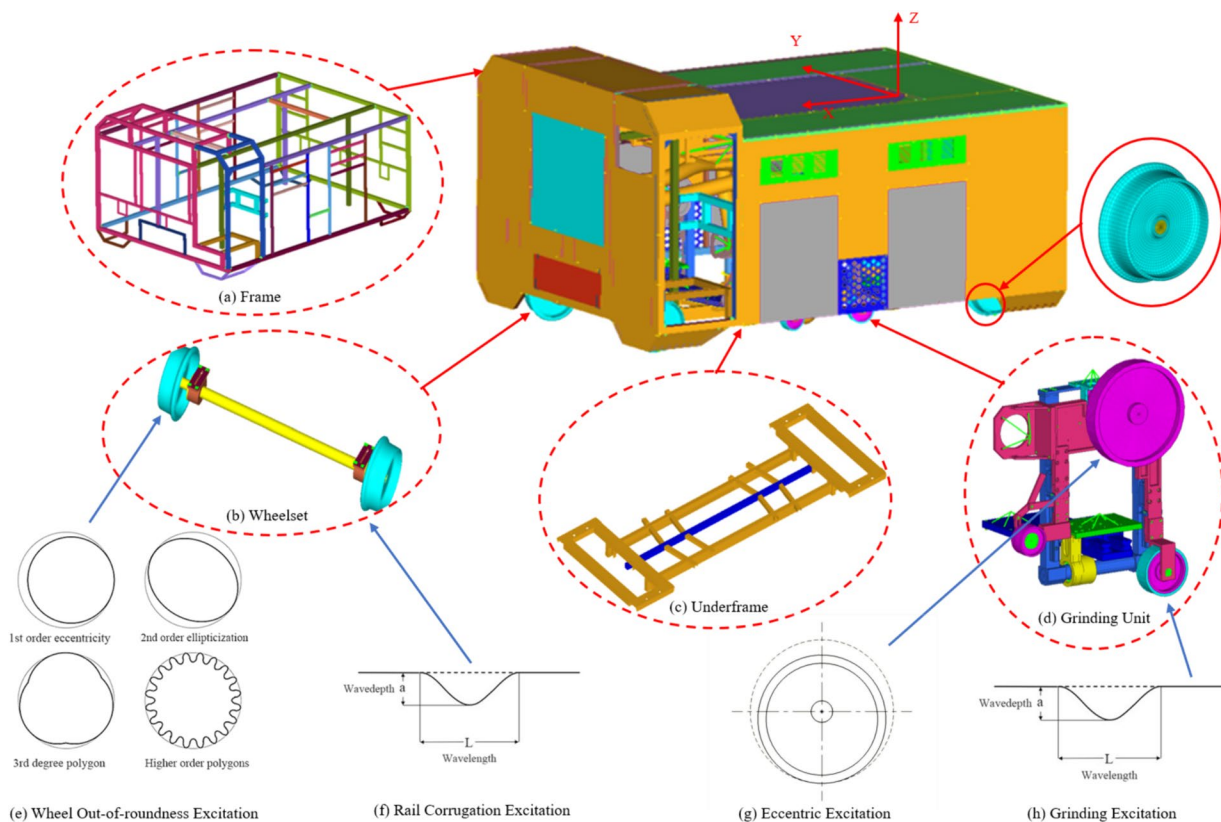
Figure 1 Finite element model and excitation

Fan *et al. Chinese Journal of Mechanical Engineering*   (2024) 37:68

Page 4 of 27

Hz at the highest speed in the non-operating state and the excitation range of the track is 18.52 to 55.56 Hz at the highest speed in the operating state.

Figure 1(g) shows the driving wheel eccentric excitation. According to the unbalance inertia force, periodic disturbance force, and transmission ratio formula in the study of Yu [5], related parameters are set as follows: the wheel (d1 = 125 mm; d2 = 180 mm), the mass of the driving wheel = 8 kg, and the eccentricity = 1 mm. The frequency range of eccentric excitation is 0 to 35 Hz and the range of inertial force is 0 to 380.65 N.

2.2 Modal Analysis of Key Components

The modes of key components are analyzed with a detailed large model as follows.

2.2.1 Modal Analysis of the Underframe

The underframe is important in the whole vehicle. After the restraint is imposed at the installation position where the underframe and the traveling part are connected,

the first 20 restraint modes of the underframe of the rail grinding vehicle with abrasive belt are calculated and the natural frequencies of the first 8 orders are listed in Table 2. The corresponding modes are shown in Figure 2.

According to Table 2 and Figure 2, the first eight natural frequencies are all within the internal and external excitation source frequency range of 0 to 111.11 Hz, so the underframe resonates when the grinding vehicle passes through rail corrugation excitation under operating conditions. As indicated in the modes of each order, the resonance parts are mainly the *Z*-direction beam in the middle of the underframe and the connection between *Z*-direction beam in the middle and the front and rear ends.

2.2.2 Modal Analysis of Frame

The frame of the rail grinding vehicle with abrasive belt is connected to the underframe through the main beam. After applying constraints at the connection installation position between the frame and the underframe, the first

Table 2 Constraint modal parameters of the underframe of the grinding vehicle

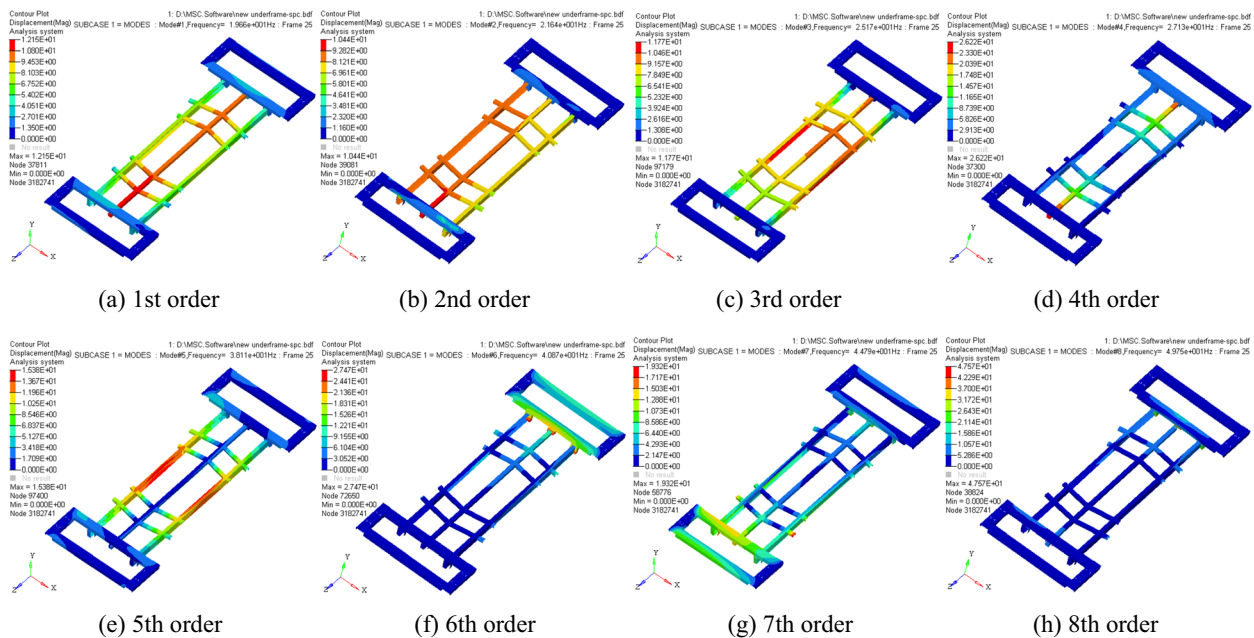| Orders	Frequencies (Hz)	Modes	Orders	Frequencies (Hz)	Modes
1	19.66	*Z*-direction vibration in the middle of *Z* direction beam	5	38.11	Twist in the middle of *Z*-direction beam
2	21.64	*Y*-direction vibration in the middle of *Z* direction beam	6	40.87	*Z*-direction fluctuations at the connection
3	25.17	Twist in the middle of *Z*-direction beam	7	44.79	Front end *Z*-direction fluctuation
4	27.13	*Z*-direction fluctuations at the connection	8	49.75	*Z*-direction fluctuations at the connection

(a) 1st order   (b) 2nd order   (c) 3rd order   (d) 4th order

(e) 5th order   (f) 6th order   (g) 7th order   (h) 8th order

Figure 2 Constrained mode diagram of the underframe of the grinding vehicle

Fan *et al. Chinese Journal of Mechanical Engineering* (2024) 37:68

Page 5 of 27

20 constrained modes of the grinding vehicle frame are calculated. Due to the dense modal frequencies, the natural frequencies of the first 10 orders are listed in Table 3 and the corresponding modes are shown in Figure 3.

According to Table 3 and Figure 3, the natural frequencies of the first ten orders are all larger than the first-order natural frequency and within the excitation source frequency range of 0 to 111.11 Hz, thus causing the frame to resonate when the grinding vehicle passes through the wave grinding under grinding operations. The mode indicates that the main part of the resonance is in the middle of the main beam of frame.

Table 3 Constraint modal parameters of the grinding vehicle frame

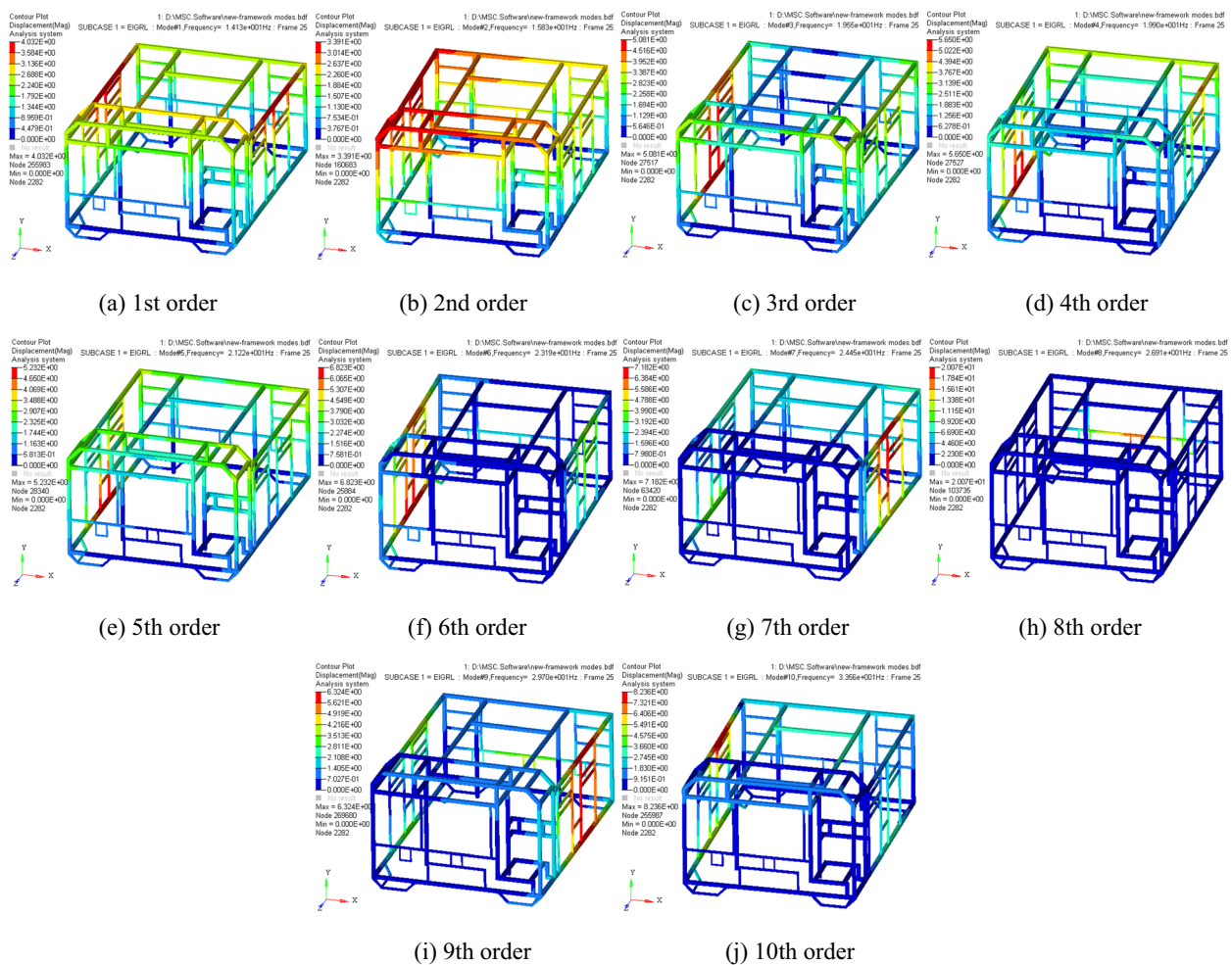| Orders	Frequencies (Hz)	Modes	Orders	Frequencies (Hz)	Modes
1	14.13	*Y*-direction vibration of left and right beams	6	23.19	Partial vibration of right frame
2	15.83	Front frame partial vibration	7	24.45	Partial vibration of left frame
3	19.55	Partial vibration of right frame	8	26.91	Partial vibration of rear frame
4	19.90	Partial vibration of right frame	9	29.70	Partial vibration of left frame
5	21.22	Partial vibration of right frame	10	33.56	Partial vibration of right frame

(a) 1st order   (b) 2nd order   (c) 3rd order   (d) 4th order

(e) 5th order   (f) 6th order   (g) 7th order   (h) 8th order

(i) 9th order   (j) 10th order

Figure 3 Constrained mode diagram of the frame of the grinding vehicle

Fan *et al. Chinese Journal of Mechanical Engineering*   (2024) 37:68

Page 6 of 27

2.2.3 Modal Analysis of the Wheelset

After the wheelset bearing seat is constrained, the first 20 constrained modes of the contact wheelset are calculated. Table 4 lists the first six vibration modes and the corresponding mode shapes are shown in Figure 4.

According to Table 4 and Figure 4, the first-order modal frequency of the wheelset is still in the excitation source frequency range of 0 to 111.11 Hz, thus causing resonance when the grinding vehicle passes through the wave grinding at a high speed. The resonance part is the wheel.

2.2.4 Modal Analysis of the Grinding Unit

After applying constraints on the grinding unit fixing frame, the first 20 constrained modes of the grinding unit are calculated. Table 5 lists some typical modal parameters, and the corresponding modal shapes are shown in Figure 5.

According to Table 5 and Figure 5, the first-order natural frequency is 3.028 Hz and the excitation source frequency is in the range of 0 to 111.11 Hz, thus causing the grinding unit to resonate when the grinding vehicle passes through the wave grinding under grinding

Table 4 Constraint modal parameters for contact wheel sets

Orders	Frequencies (Hz)	Modes	Orders	Frequencies (Hz)	Modes
1	74.92	Wheel radial expansion	4	271.50	Wheel radial fluctuation
2	118.60	Wheel corners flared	5	305.70	Fluctuation of the wheel
3	183.00	Z-direction axle bends	6	426.10	Wheel radial expansion

(a) 1st order   (b) 2nd order   (c) 3rd order   (d) 4th order
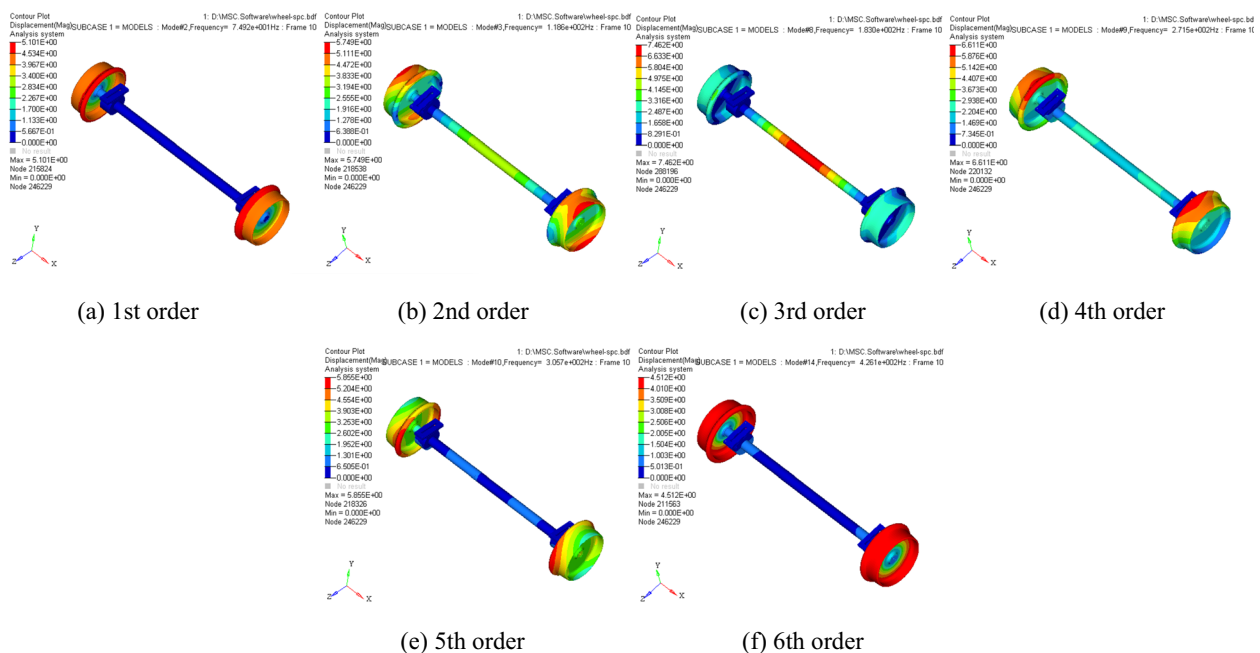
(e) 5th order   (f) 6th order

Figure 4 Constraint mode diagram of the contact wheel set

Table 5 Constraint modal parameters of the grinding unit of the grinding vehicle

Orders	Frequencies (Hz)	Modes	Orders	Frequencies (Hz)	Modes
1	3.028	Contact wheel partial mode	9	28.88	Drive wheel partial mode
3	4.460	First-order twist	12	36.42	Frame partial mode
5	6.198	Tension pulley partial mode	16	56.64	Tension pulley partial mode
6	14.28	Tension pulley partial mode	17	60.92	Frame partial mode

(a) 1st order   (b) 3rd order   (c) 5th order   (d) 6th order

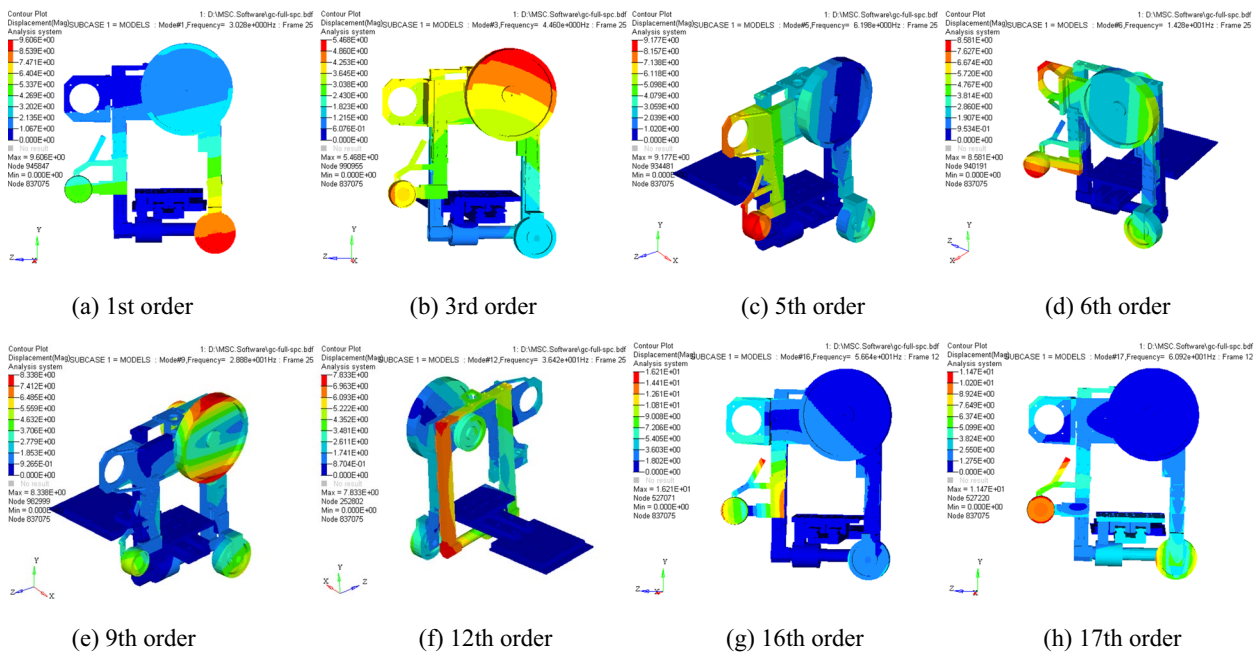(e) 9th order   (f) 12th order   (g) 16th order   (h) 17th order

Figure 5 Constrained mode diagram of the grinding unit

operations. The mode shape indicates that the resonance parts are mainly the mounting brackets of driving wheel, tension wheel, and contact wheel.

2.3 Modal Analysis of the Vehicle

The first 20 free modes of the grinding vehicle are calculated. Table 6 lists some non-zero modal parameters and the corresponding mode shapes are shown in Figure 6.

According to Table 6 and Figure 6, the first six-order non-zero modal frequency is low and the seventh-order natural frequency of 2.277 Hz is in the excitation source frequency range of 0 to 111.11 Hz, thus causing the grinding vehicle to resonate as it passes through the rail corrugation under operating conditions. Among the resonance frequencies, the low-order frequency is mainly caused by the out-of-roundness of the wheel.

When the grinding vehicle is running and grinding normally, the excitation frequencies of the other main excitation sources are much higher than the seventh-order natural frequency of the grinding vehicle. In the modes, the grinding unit has many partial modes, indicating that

the rigidity at the connection between grinding unit and underframe and the connection between wheelset and underframe is low.

3 Dynamic Performance Analysis

Dynamic characteristics are the basis for studying vibration control of grinding vehicles. The vibration of the grinding vehicle is analyzed through frequency response simulation and transient dynamic response simulation.

3.1 Frequency Response Analysis

Six reference points are selected at each key part of the grinding vehicle to analyze the acceleration response in the frequency domain, as shown in Figure 7.

3.1.1 Rail Corrugation Excitation

After the rail corrugation excitation is applied, the vibration response of the vehicle in the frequency range of 18.52 to 111.11 Hz is analyzed. The selected four reference points are shown in Figure 7. The acceleration

Table 6 Free modal parameters of the whole grinding vehicle

Orders	Frequencies (Hz)	Modes	Orders	Frequencies (Hz)	Modes
7	2.277	Grinding element partial mode	10	2.703	Electrical rack partial mode
8	2.357	First-order twist	11	3.081	Grinding element partial mode
9	2.563	Electrical rack partial mode	12	3.819	Vibration at the front of the vehicle

| (a) 7th order | (b) 8th order | (c) 9th order | (d) 10th order |

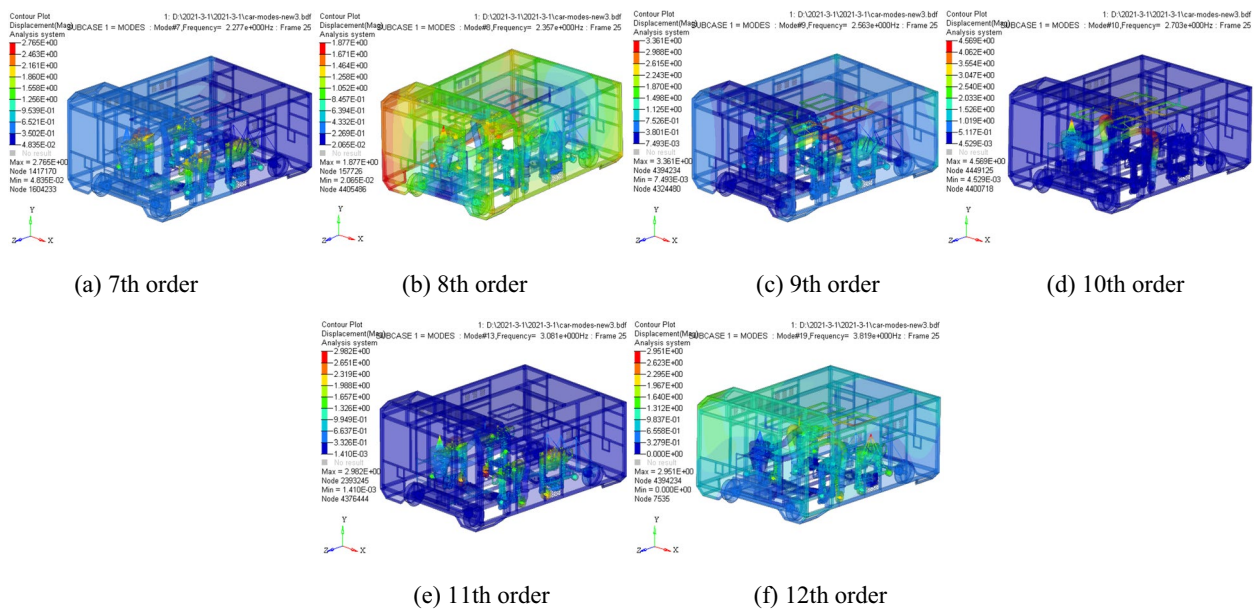| (e) 11th order | (f) 12th order |

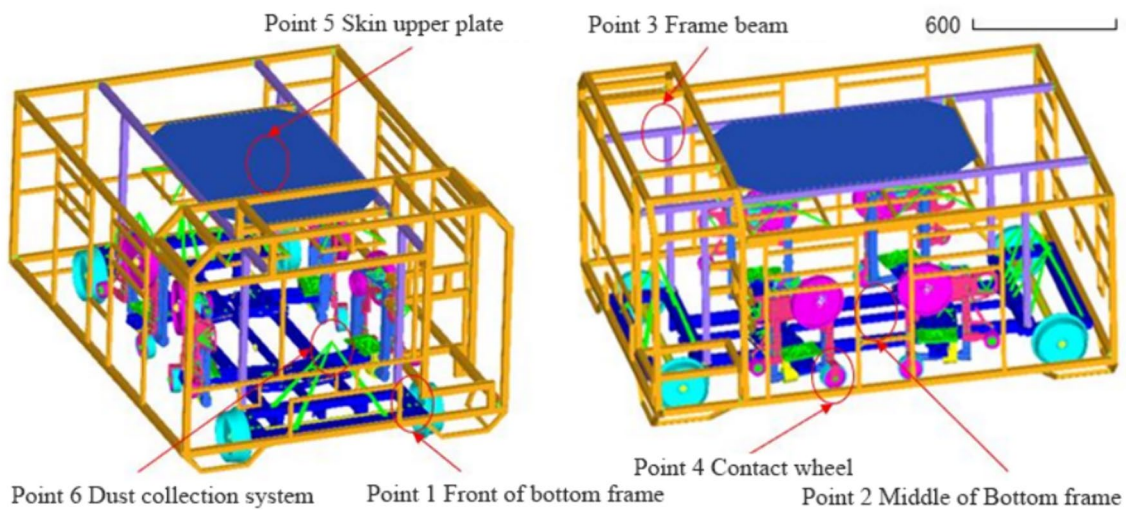**Figure 6** Free-mode vibration mode diagram of the whole grinding vehicle

Figure 7 Schematic diagram of the selected six reference points

response results of each reference point are extracted (Figure 8).

As shown in Figure 8, the frequency range of rail corrugation excitation is between 17 and 112 Hz. The overall trend of each reference point is introduced below. The vibration acceleration in the three directions gradually increases with the increase in the frequency and the Y-direction vibration is the main vibration. When the frequency is above 50 Hz, the vibration of the whole vehicle is large. In other words, the grinding vehicle generates

large vibrations under the fast speed or short-wave grinding conditions.

3.1.2 Wheel Out-of-Roundness Excitation

After the wheel out-of-round excitation is applied, the vibration response of the vehicle at the 1st-3rd order of excitation frequencies of the wheel polygon is analyzed. The selected reference points are shown in Figure 7 and the acceleration response results of each reference point are extracted (Figure 9).
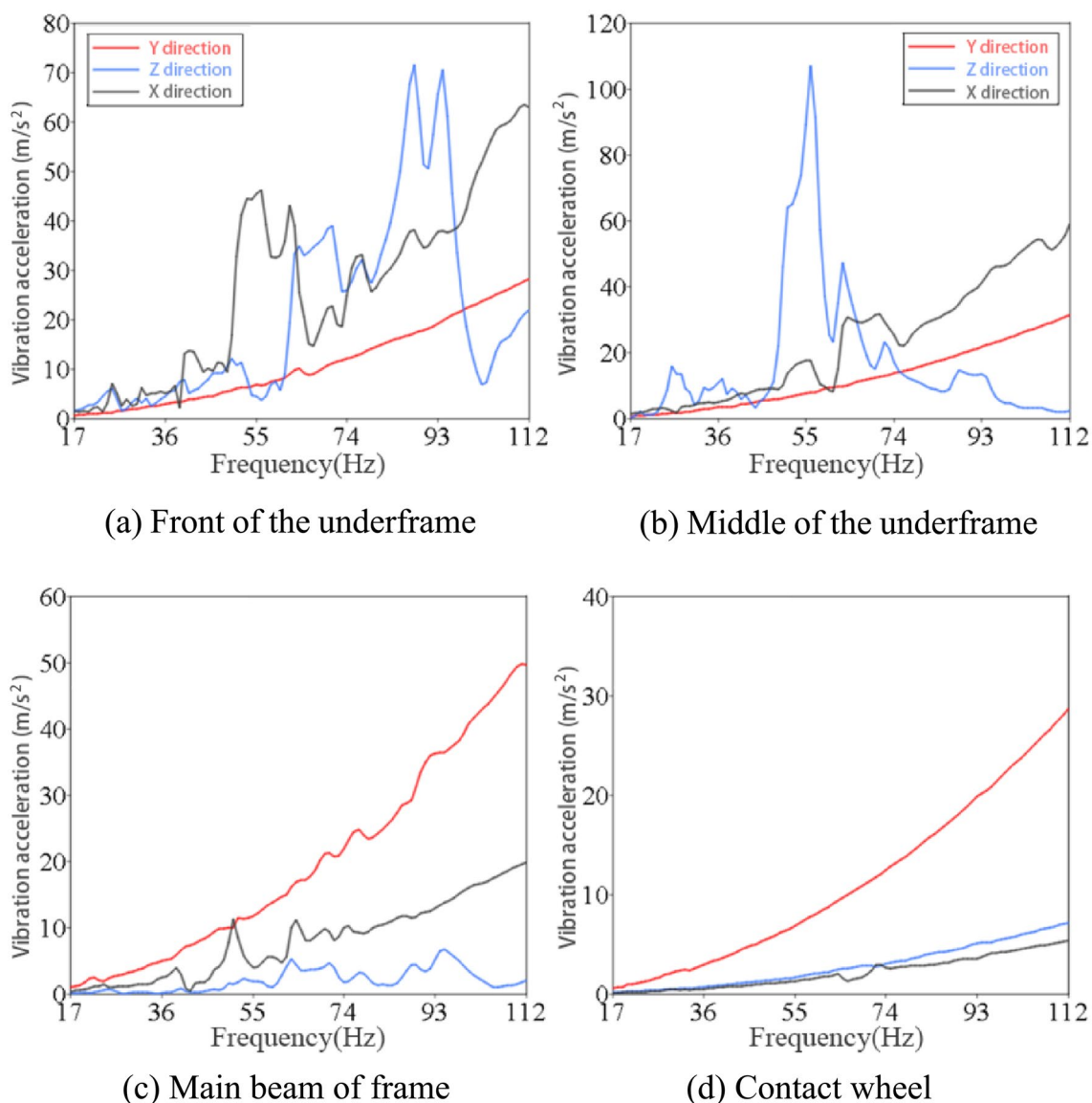
(a) Front of the underframe

(b) Middle of the underframe

(c) Main beam of frame

(d) Contact wheel

Figure 8 Frequency domain diagram of vibration acceleration at each reference point under rail corrugation excitation

As shown in Figure 9, the wheel out-of-round excitation frequency range is between 0 and 15 Hz and belongs to the low frequency range, thus causing the resonance of the whole vehicle. Among the 4 reference points, the vibration of the contact wheel and the middle of the underframe is relatively large. The vibration amplitude increases gradually with the increase in the frequency and peaks at approximately 14 Hz. By improving the structure of the underframe and increasing the rigidity, the vibration problem caused by the out-of-roundness of the wheel can be avoided.

3.1.3 Abrasive Belt Grinding Excitation
After the abrasive belt grinding excitation is applied, the vibration response of the vehicle in the excitation frequency range of 18.52 to 55.56 Hz is analyzed. The selected four reference points are shown in Figure 7 and the acceleration response results of each reference point are extracted (Figure 10).

As shown in Figure 10, the excitation frequency range of abrasive belt grinding is between 17 and 55 Hz. The vibration acceleration of each reference point gradually increases with the increase in the frequency and the
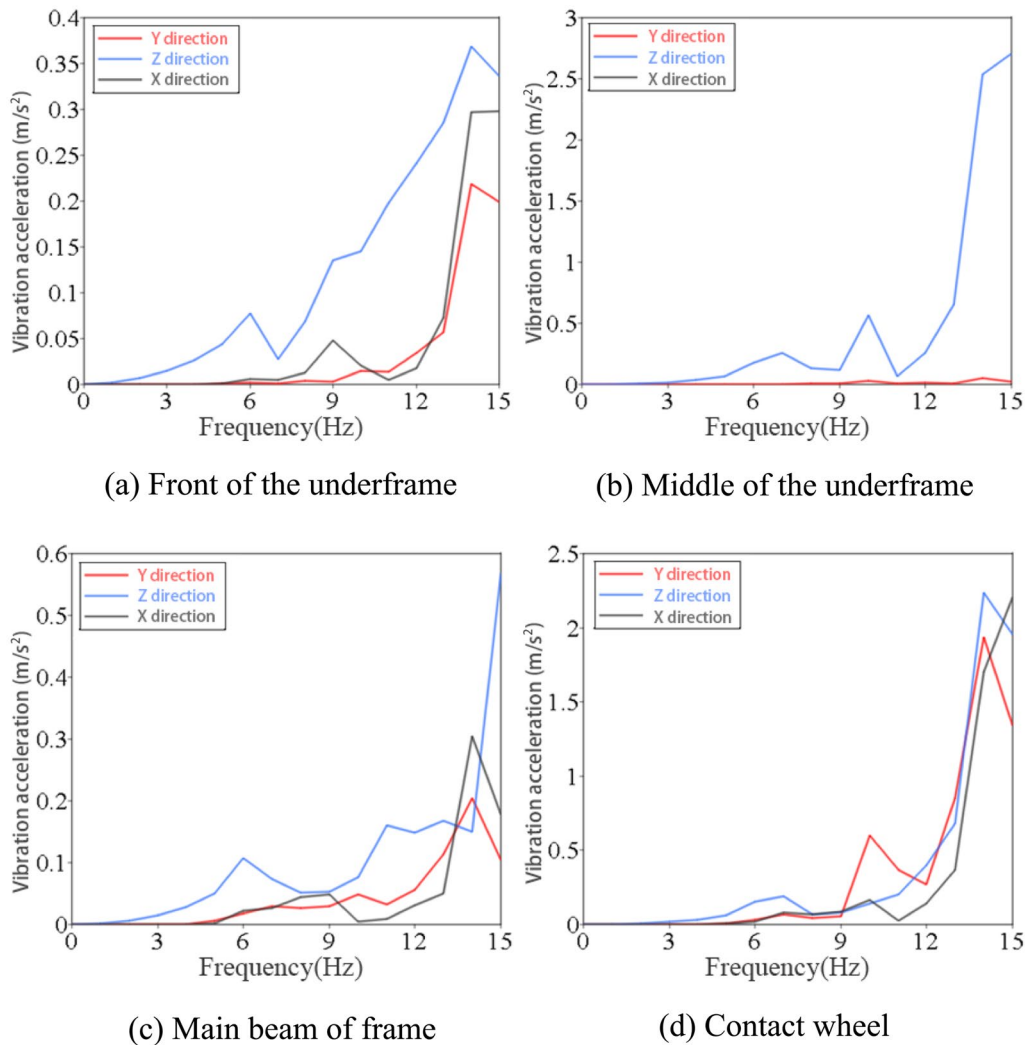
(a) Front of the underframe

(b) Middle of the underframe

(c) Main beam of frame

(d) Contact wheel

Figure 9 Frequency domain diagram of vibration acceleration at each reference point under wheel out-of-roundness excitation

vibration generated by grinding is transmitted to each reference point through the grinding unit mounting plate. The vibration of the main beam of frame is similar to that of the front end of underframe. Resonance occurs the when *X*-direction vibration frequency is 45 Hz.

3.1.4 Driving Wheel Eccentric Excitation

Eccentric excitation is applied in order to analyze the vibration response of the vehicle at an excitation frequency of 0 to 35 Hz. The selected four reference points are shown in Figure 7 and the acceleration response results of each reference point are extracted (Figure 11).

As shown in Figure 11, the acceleration response frequency of each component is concentrated in the range between 25 Hz and 35 Hz. Resonance is generated near 33 Hz and a vibration peak occurs. The result may be interpreted as follows. The inertial force generated by

the eccentricity of the driving wheel increases with the increase in the rotational speed of the driving wheel, thus resulting in an increase in the overall vibration. Therefore, it is necessary to correct the eccentricity of the driving wheel of the grinding unit so as to avoid violent vibration.

3.2 Dynamic Performance Analysis

The grinding vehicle is subjected to various excitation combinations during driving and operation, so various excitation sources are applied according to the actual operating conditions in the simulation analysis. Under non-operating conditions, the grinding vehicle is subjected to rail corrugation excitation and wheel out-of-roundness excitation. Under operating conditions, the grinding vehicle is additionally subjected to grinding excitation and drive wheel eccentric excitation.
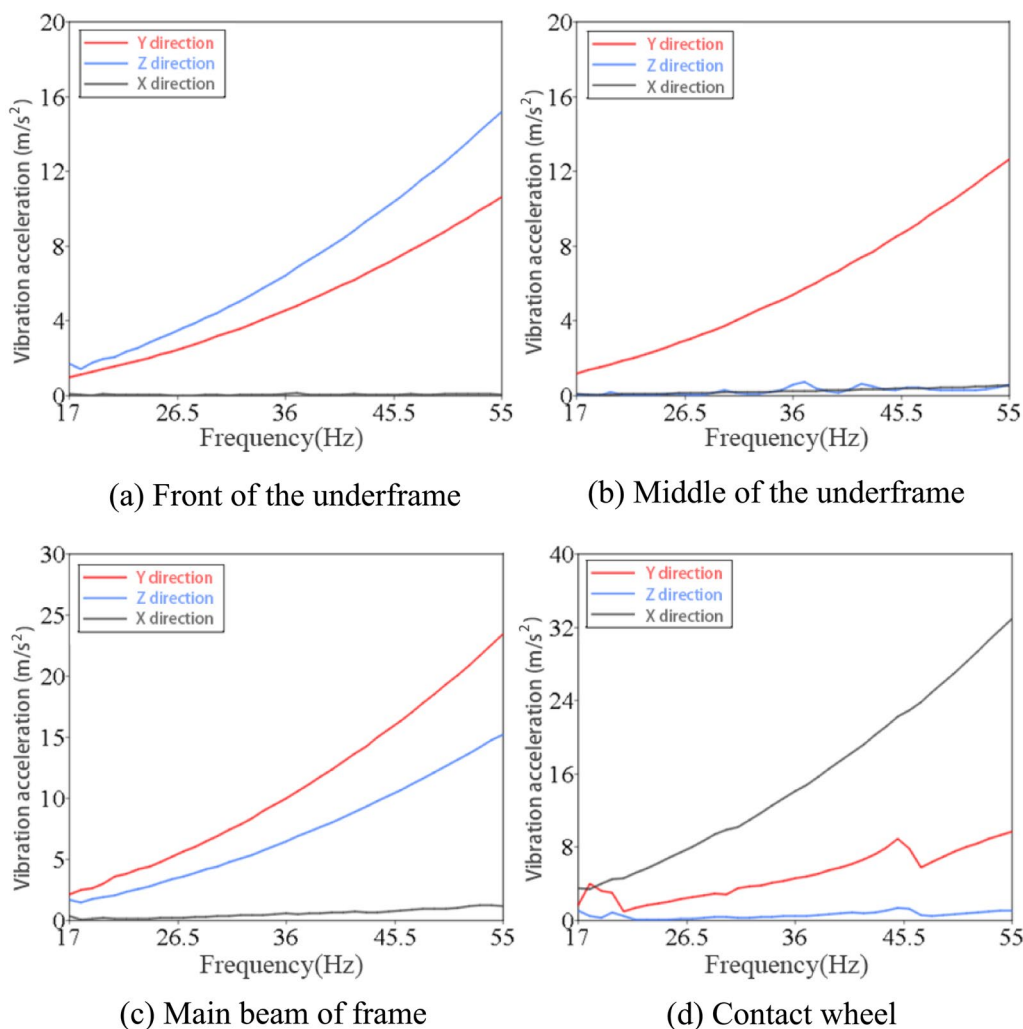
(a) Front of the underframe

(b) Middle of the underframe

(c) Main beam of frame

(d) Contact wheel

Figure 10 Frequency domain diagram of vibration acceleration at each reference point under abrasive belt grinding excitation

3.2.1 Non-operating Conditions

Under non-operating conditions, the grinding vehicle runs on the rail without grinding. The driving speed is higher than that under operating conditions. The excitation source is the rail corrugation excitation and the wheel out-of-round excitation (Table 11). In the transient response analysis under non-operating conditions, the input includes the multiple cycles of rail corrugation excitation with the frequency of 111.11 Hz and wheel out-of-round excitation with the frequencies of 4.78 Hz, 9.56 Hz, and 15 Hz, as shown in Figure 12.

The selected reference points are shown in Figure 7 and the vibration acceleration time domain diagram of each reference point are shown in Figure 13.

As shown in Figure 13, after the rail corrugation and the wheel out-of-round excitation are loaded, the vibration acceleration of the reference point has different numbers of peaks in the lateral, *X*- and *Z*-directions.

The result is interpreted as follows. The applied displacement excitation is a periodic simple harmonic excitation, which conforms to the characteristics of the input function. There is no bogie or suspension damping device, so the vibration acceleration of each part of the vehicle is too large.

The reference point of the front end of underframe is selected at the place where underframe and wheel are connected and installed and the most affected by vibration. The input excitation is in the *Z*-direction, so *Z*-direction acceleration is significantly greater than *X*- and *Y*-direction accelerations. The reference point of frame is located at the main beam and the connection point between the main beam and the underframe is close to the bearing seat, so the vibration is similar to that at the front end of the underframe. The *Z*-direction vibration is the most obvious and *X*- and *Y*-direction vibrations are small. Due to the vibration transmitted by

(a) Front of the underframe

(b) Middle of the underframe
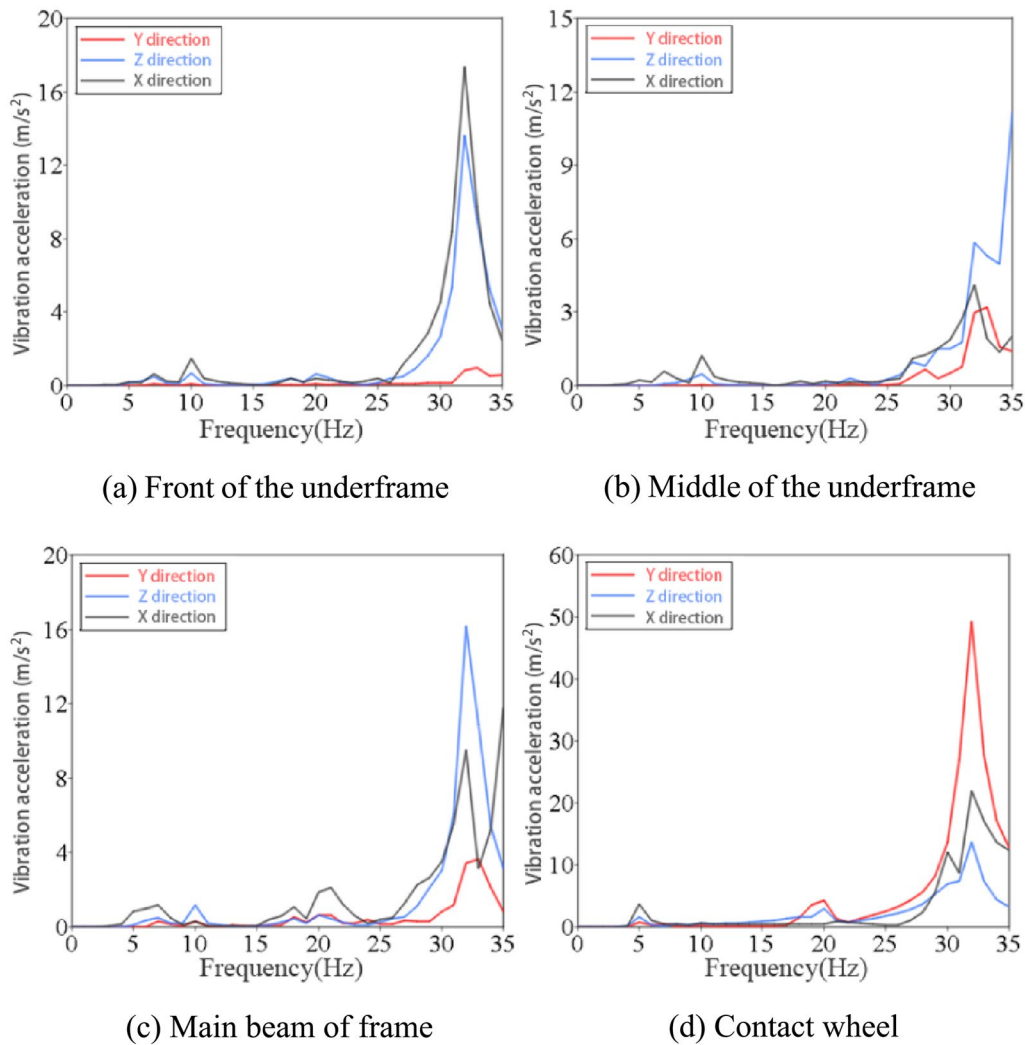
(c) Main beam of frame

(d) Contact wheel

Figure 11 Frequency domain diagram of vibration acceleration at each reference point under eccentric excitation
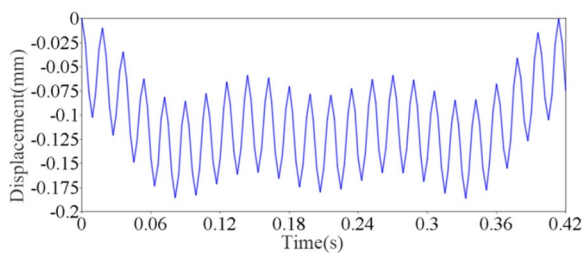

Figure 12 Time domain diagram of displacement excitation under non-operating conditions

the frame, Z-direction vibration of the upper panel of the skin is more obvious than X- and Y-direction vibrations. The dust collection system is installed on the front end of the underframe and greatly affected by Z-direction vibration of the front end of the underframe, so the main vibration of the dust collection system is the Z-direction vibration.

Fast Fourier transform is performed on the time-domain diagram of vibration acceleration to obtain the frequency-domain diagram of vibration acceleration (Figure 14).

As shown in Figure 14, the acceleration response frequency of the reference point is mainly concentrated in the range of 0 to 200 Hz. The acceleration response curve of the front end of underframe has the peaks in three directions mainly at 113 Hz and 184 Hz. The frequency of 113 Hz coincides with the vibration frequency of 111.11 Hz excited by rail corrugation and the frequency of 184 Hz coincides with the Z-direction bending modal frequency of wheelset axle (183 Hz), thus causing resonance. The most significant acceleration response peaks

(a) Front of the underframe

(b) Middle of the underframe

(c) Main beam of frame

(d) Contact wheel

(e) Skin upper plate
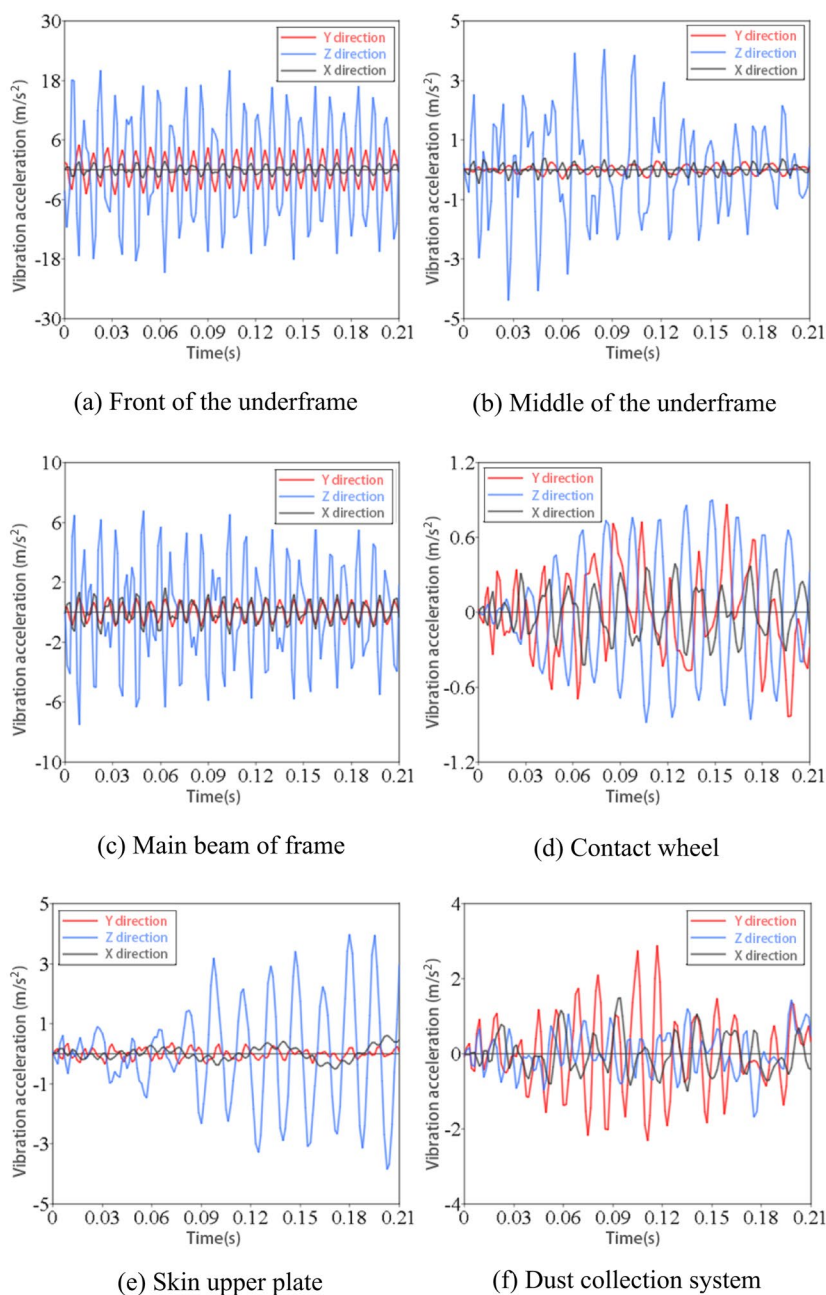
(f) Dust collection system

Figure 13 Time domain diagram of vibration acceleration at each reference point under non-operating conditions

of the main beam of frame are also at 113 Hz and 184 Hz. The vibration response principle of the main beam of frame is similar to that of the front end of underframe.

The peak acceleration response in the middle of underframe is mainly at the frequencies of 61 Hz, 113 Hz, and 165 Hz. The frequency of 61 Hz is close to the Z-direction bending modal frequency of Z-direction beam of underframe, 62.50 Hz. The frequency of 113 Hz is close to the vibration frequency of the rail corrugation excitation of 111.11 Hz. The frequency of 165 Hz

is close to the wave modal frequency of the Z-direction beam stiffener of underframe (160 Hz), so resonance occurs.

The frequency of the vibration response peak of contact wheel of the grinding unit (61 Hz) is close to the natural modal frequency of the grinding unit (60.92 Hz) and the mode is the partial mode of the deflection mechanism support frame. The vibration frequency of skin is mainly below 100 Hz and the Z-direction vibration is the main vibration and peaks at 61 Hz.
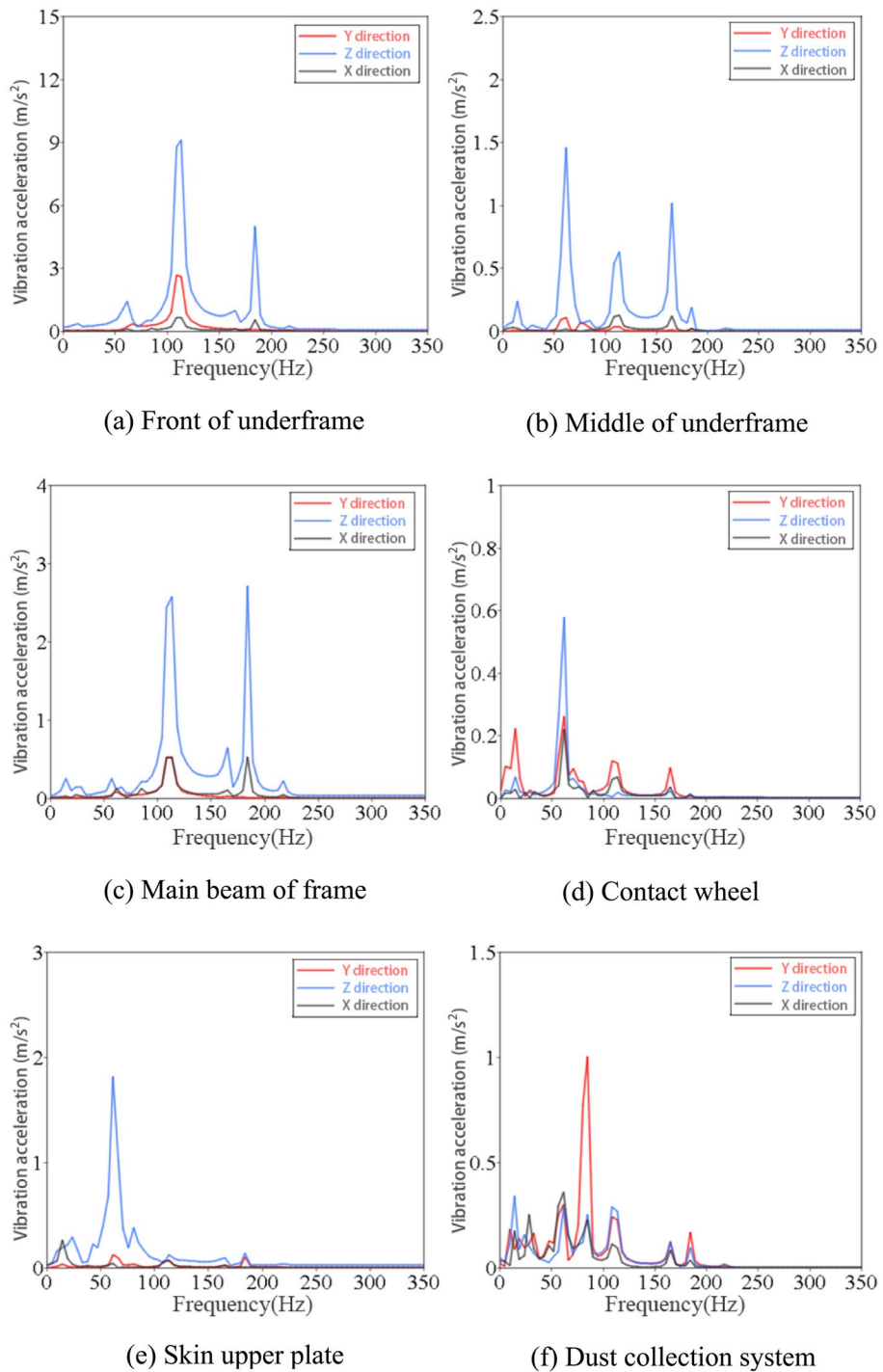
(a) Front of underframe

(b) Middle of underframe

(c) Main beam of frame

(d) Contact wheel

(e) Skin upper plate

(f) Dust collection system

Figure 14 Frequency domain diagram of vibration acceleration at each reference point under non-operating conditions

3.2.2 Operating Conditions

Under the grinding condition, the grinding vehicle runs on the rail and performs the grinding operation. The excitation sources are rail wave grinding, wheel out-of-round excitation, grinding excitation, and eccentric excitation.

According to the frequency response analysis of a single excitation source, the rail corrugation excitation and abrasive belt grinding excitation occur at the input frequency of 55.56 Hz under the grinding operation condition. The wheel out-of-round excitation occurs at the

frequencies of 3 Hz, 6 Hz, and 9 Hz and the active excitation of wheel eccentric excitation occurs at 35 Hz, as shown in Figure 15.

The selected reference points are shown in Figure 7. The time domain diagram of vibration acceleration at each reference point is shown in Figure 16.

The reference *Z*-direction acceleration of the front end of underframe is significantly greater than *X*- and *Y*-direction accelerations (Figure 16). When the corrugation excitation occurs at the frequency of 55 Hz, *X*-direction resonance of the front end of underframe occurs and is more severe than that at 111.11 Hz under non-operating conditions. Under operating conditions, the bearing seat is also subjected to the abrasive belt grinding excitation transmitted by underframe and the eccentric excitation of driving wheel, so *X*- and *Z*-direction vibrations are larger than those under non-operating conditions.

The frame is mainly subjected to various vibrations transmitted from the underframe and *X*- and *Z*-direction vibrations are the most obvious. The grinding unit vibrates violently because the reference point of the

(a) Rail corrugation and wheel out-of-round excitation

(b) Belt grinding excitation

(c) Drive wheel eccentric excitation

Figure 15 Time domain diagram of excitation under operating conditions

grinding unit is set on the contact wheel. The vibration of the grinding unit is directly affected by the abrasive belt grinding excitation and the eccentric excitation of driving wheel. *X*- and *Y*-direction vibrations of contact wheel are significant and *X*-direction vibration is the most significant after reaching a steady state. The *Z*-direction vibration of skin upper plate is stronger than *X*- and *Y*-direction vibrations and the overall vibration is larger than that under the non-operating condition. The vibration of dust collection system is obviously enhanced because the dust collection system is installed on the underframe and the vibration of underframe causes a large vibration of dust collection system.

Fast Fourier transform is performed on the time-domain diagram of vibration acceleration to obtain the frequency-domain diagram of vibration acceleration (Figure 17).

As shown in Figure 17, the vibration response frequency of each component is mainly concentrated in the range of 0 to 120 Hz, which is consistent with the frequency range of natural mode and excitation source.

The acceleration response curve of the front end of underframe has the peaks at 35 Hz and 55 Hz in three directions. The frequency of 35 Hz coincides with the eccentric excitation frequency of the drive wheel and the frequency of 55 Hz coincides with the rail corrugation excitation frequency and the abrasive belt grinding excitation frequency, thus causing resonance. The acceleration response curve in the middle of underframe also has the peaks at 34 Hz and 54 Hz in three directions, similar to that of the front end of underframe.

The acceleration response peaks of the main beam of frame also occur at the frequencies of 34 Hz and 54 Hz. The main beam is less affected by the excitation source than the underframe due to the transmission through the underframe. The acceleration response peaks of contact wheel occur at 34 Hz, 40 Hz, and 54 Hz, and *X*- and *Y*-direction acceleration peaks occur at 34 Hz, indicating that the eccentric excitation of driving wheel is mainly transmitted laterally and longitudinally to the contact wheel. The skin vibration is still dominated by *Z*-direction vibration under operating conditions and the rail corrugation excitation at 55 Hz has a significant impact on skin. The vibration of dust collection system is dominated by *Z*-direction vibration with a peak at 34 Hz and mainly affected by the eccentric excitation of driving wheel of the grinding unit.

3.3 Vibration Evaluation

By calculating the root mean square (RMS) value of vibration acceleration in the time domain, the vibration strength of the whole vehicle and key components can be judged. In this part we will calculate RMS of vibration
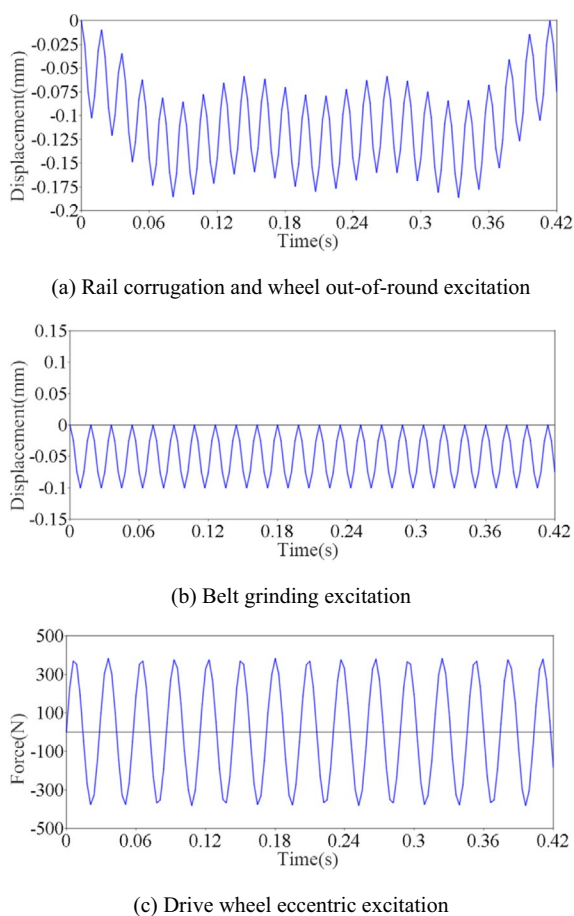
(a) Front of underframe

(b) Middle of underframe

(c) Main beam of frame

(d) Contact wheel

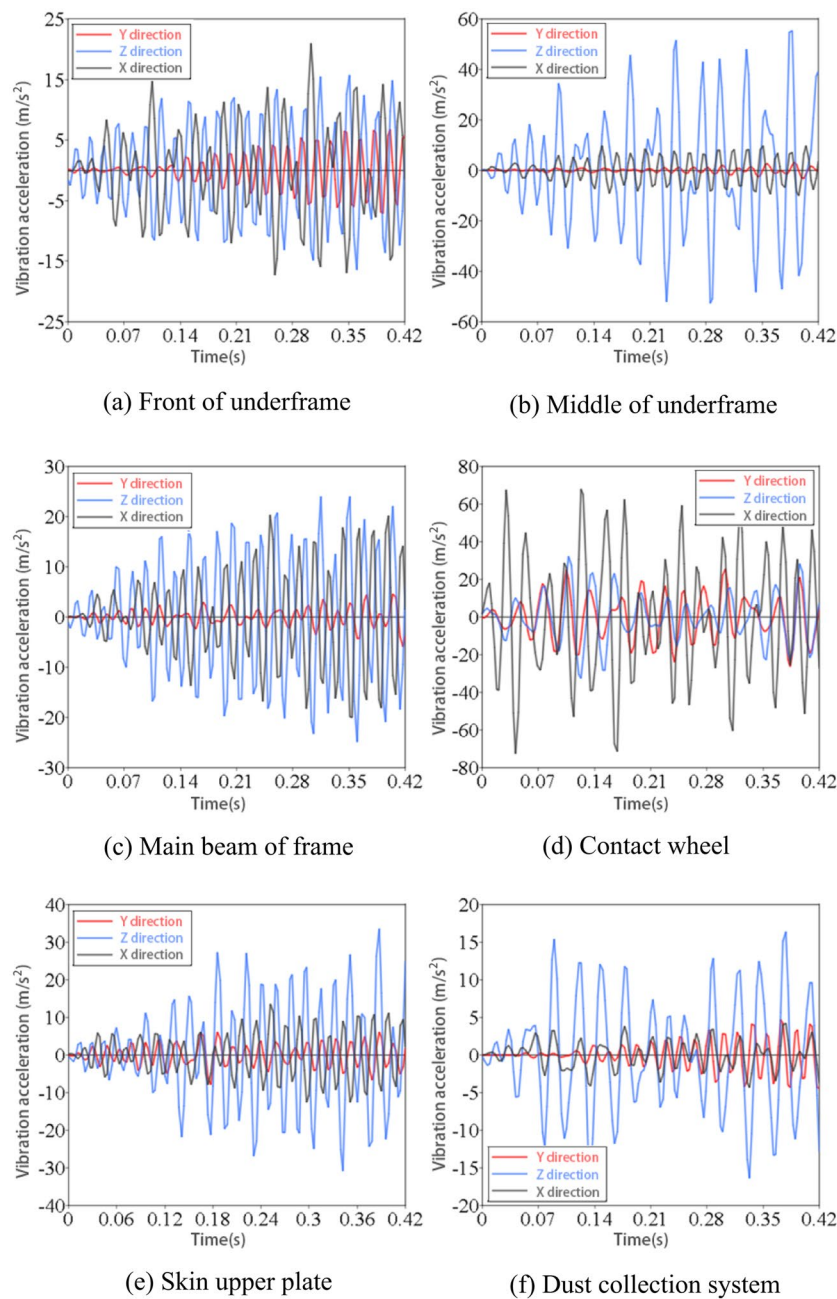(e) Skin upper plate

(f) Dust collection system

Figure 16 Time domain diagram of vibration acceleration at each reference point under operating conditions

acceleration of three directions and all reference points of the whole vehicle in three directions by 6 reference points.

3.3.1 Non-operating Conditions

From the dynamic response analysis results of the above symmetrical grinding non-operating conditions, the vibration acceleration at each reference point is extracted

and RMS value of vibration acceleration at each reference point is calculated, as shown in Table 7.

According to the GB/T 17426-1998 standard [39] (hereinafter referred to as GB/T 17426-1998), the maximum Z-direction vibration acceleration of special railway vehicles and rail machinery is 6.87 m/s^2 and X-direction vibration acceleration is 4.91 m/s^2. Due to the large size of the model and insufficient computer calculation capability, the experimental section in the simulation analysis
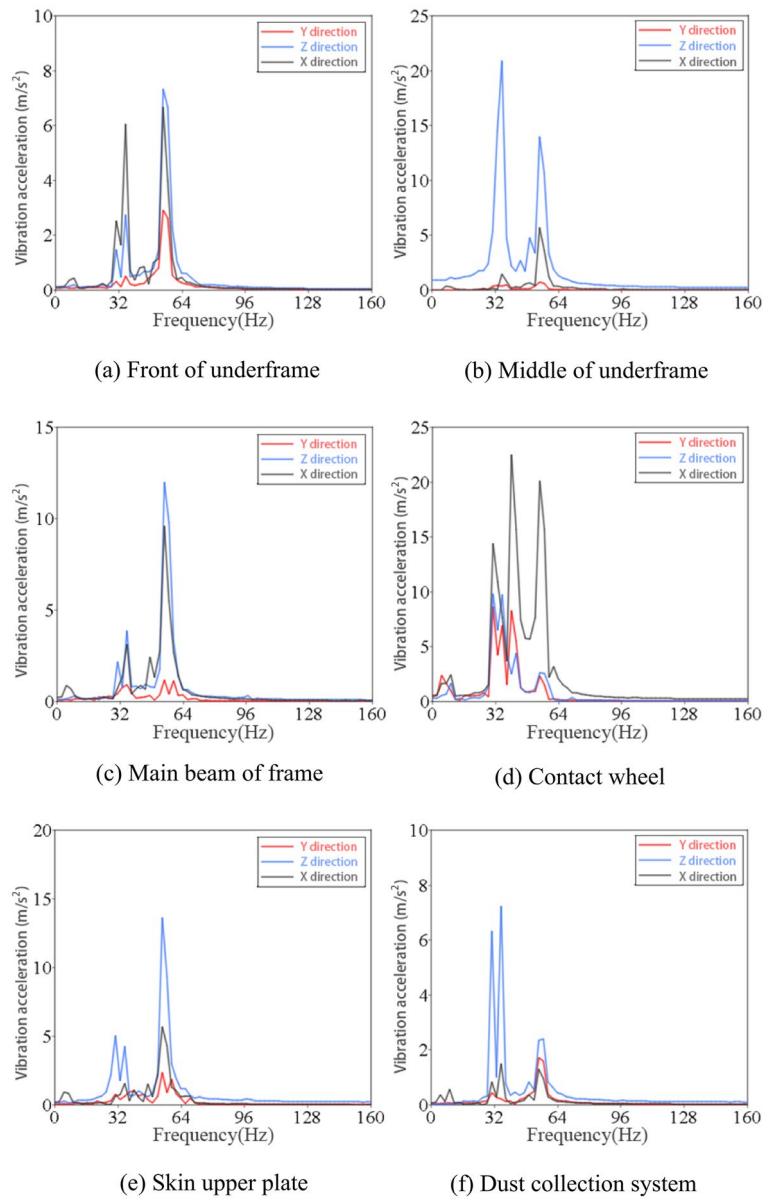
(a) Front of underframe

(b) Middle of underframe

(c) Main beam of frame

(d) Contact wheel

(e) Skin upper plate

(f) Dust collection system

Figure 17 Frequency domain diagram of vibration acceleration at each reference point under operating conditions

Table 7 Effective values of vibration acceleration at the reference point of each component under non-operating conditions

Directions	Front of underframe	Middle of underframe	Main beam of frame	Contact wheel	Skin upper plate	Dust collection system
X-direction	2.9389	0.1317	0.5873	0.3374	0.1653	1.0366
Y-direction	10.6702	1.5933	3.4995	0.4651	1.7110	0.5575
Z-direction	0.8582	0.1720	0.7234	0.1901	0.2269	0.5064
Average	4.8224	0.6323	1.6034	0.3308	0.7010	0.7001

is short. Therefore, the average vibration acceleration in this section is calculated to represent the vibration acceleration of the 100-km test section in GB/T 17426-1998.

According to Table 7, the *Z*-direction vibration acceleration of the front end of chassis is 10.67 m/s^2, which does not meet the maximum vibration acceleration specified in GB/T 17426-1998.

When the grinding vehicle is subjected to the maximum rail corrugation excitation and the underframe does not resonate under the non-operating condition, the root mean square value of vibration acceleration of the whole vehicle is calculated to be 3.20 m/s^2.

3.3.2 Operating Conditions

From the dynamic response analysis results of the above symmetrical grinding operation conditions, the vibration acceleration value of each reference point is extracted and RMS value of vibration acceleration at each reference point is calculated (Table 8).

The *Z*-direction vibration acceleration of the front end of underframe is 7.76 m/s^2 (Table 8), which does not meet the maximum *Z*-direction vibration acceleration specified in GB/T 17426-1998.

Under the grinding operation conditions, due to the actions of rail corrugation excitation, abrasive belt grinding excitation, driving wheel eccentric excitation, and the resonance of underframe, RMS of vibration acceleration of the whole vehicle is 15.60 m/s^2.

4 Structural Optimization

Based on the modal analysis results, the natural frequency of the equipment structure is changed to be far away from the main frequency of the excitation force so as to prevent resonance. The vibration control is generally implemented by setting vibration isolation elements, optimizing the structure, and increasing damping.

4.1 Vibration Isolation Element

4.1.1 Connection between Underframe and Walking Parts

The natural frequency f_0 of the vibration isolation system is calculated according to the frequency ratio $\frac{f}{f_0} = 2.5 - 5$

[40]. For rubber materials, dynamic characteristics need to be considered:

$$f_0 = \frac{5}{\sqrt{x}} \sqrt{\frac{E_d}{E_0}}, \tag{1}$$

where x is the static compression of the elastic member of the vibration isolation system under the action of equipment gravity; E_d and E_0 are the dynamic and static elastic moduli of the rubber material, respectively.

According to the natural frequency and mass required by the vibration isolation system, the stiffness and static compression of the vibration isolator are calculated as follows:

$$K = M(2\pi f_0)^2, \tag{2}$$

$$x = Mg/K. \tag{3}$$

Where K is the stiffness of the vibration isolator; M is quality; f_0 is the natural frequency; x is the amount of static compression.

According to the above dynamic response analysis, the excitation frequency of rail corrugation is above 50 Hz, so the vibration generated by the grinding vehicle is the strongest.

The natural frequency of the vibration isolation system is preliminarily determined to be 10 to 25 Hz. The 16 bolts on underframe are replaced by isolators (Position 1 shown in Figure 18). The weight of rail grinding vehicle and abrasive belt excluding running parts is approximately 1300 kg. The load of each vibration isolator is $M = 81.25$ kg. With Eq. (2), the range of stiffness K of the vibration isolation system is calculated as 3205 to 20041 N/cm. With Eq. (3), the static compression x is calculated as 2.4 to 0.4 mm.

Based on the above analysis, the compression type rubber vibration isolator is selected. With the required maximum static compression x, the material thickness and required compression or shear area are calculated below.

The material thickness is calculated as:

Table 8 Effective values of vibration acceleration at the reference point of each component under operation conditions

Directions	Front of underframe	Middle of underframe	Main beam of frame	Contact wheel	Skin upper plate	Dust collection system
X direction	2.9927	0.9421	1.6987	11.5301	2.8243	1.8458
Y direction	7.7557	23.5237	11.8953	12.3307	13.3423	7.3990
Z direction	7.5102	5.0975	9.0508	31.8419	5.8691	1.8253
Average	6.0862	8.3612	7.5426	18.5676	7.3412	3.6942

(a) Position 1   (b) Position 2

Figure 18 Schematic diagram of the positions of rubber shock absorbers

(a) Rubber isolator   (b) Finite element model

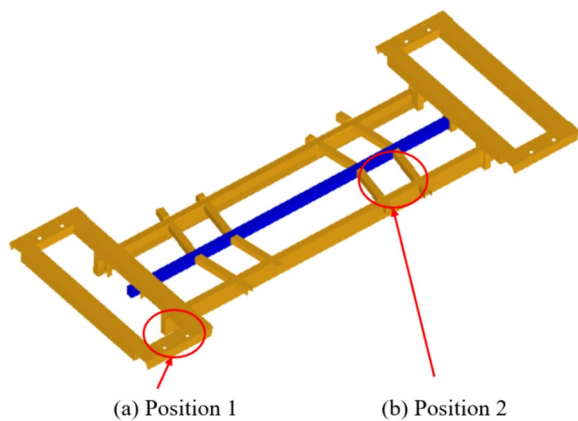**Figure 19** Schematic diagram of the rubber shock absorber

$$H = \frac{xE_d}{\sigma}, \tag{4}$$

where H is the thickness of material; E_d is the dynamic elastic modulus of the rubber; σ is the allowable load of the rubber.

The isolator footprint is expressed as:

$$S = \frac{M}{\sigma}, \tag{5}$$

where S is the supporting area of the rubber.

The constants E_d and σ of rubber are provided in Table 9 [41]. A schematic diagram of the rubber vibration isolator is shown in Figure 19.

Due to the limitation of Z-direction movement distance of the grinding unit, the thickness H of the rubber material should be as small as possible. According to Table 9 and Eq. (4), a harder rubber with $E_d/\sigma = 50$ is selected and when the static compression is 0.8 mm, H is 40 mm. According to Eq. (5), the required area is calculated as $S=406$ with the allowable pressure of the rubber vibration isolator, so $D2$ should be greater than 22 mm.

Therefore, the GXGSS5744M8 rubber vibration isolator made of galvanized Q235 carbon steel and natural rubber is selected. The maximum load is 95 kg. The thickness H is 44 mm and the diameter of the rubber material is 57 mm.

4.1.2 Connection between Grinding Unit and Underframe

The excitation sources at the installation position where grinding unit and underframe are connected are mainly the eccentric excitation of driving wheel and the abrasive belt grinding excitation (Position 2 in Figure 18) and the frequency range is 18.52 to 55.56 Hz.

The natural frequency f_1 of the vibration isolation system is preliminarily determined to be 6 to 15 Hz. The underframe is connected to the grinding unit through the mounting plate with 6 bolts, which are replaced with 6 vibration isolators. The weight of grinding unit is approximately 80 kg. The load of each isolator is $M' = 13.3$ kg. With Eq. (2), the stiffness range K' of the vibration isolation system is calculated as 186 to 1176 N/cm. With Eq. (3), the static compression amount x' is calculated as 7 to 1.1 mm.

Additionally, the above type of rubber vibration isolator is chosen. Due to the limitation of Z-direction movement distance of the grinding unit, the thickness H' of the rubber material should be as small as possible. According to Table 9 and Eq. (4), soft rubber $E_d/\sigma = 25$ is selected. When the static compression x' is 1.1 mm, H' is 27.5 mm. With Eq. (5), the required area is calculated as $S=66.5$ based on the allowable pressure of the rubber vibration isolator. Therefore, the GXGSS2015M6 rubber vibration isolator made of galvanized Q235 carbon steel and natural rubber is selected. The maximum load is 15 kg. The thickness H is 15 mm and the diameter of the rubber material is 20 mm

Table 9 Parameters of common rubbers

Materials	Poisson's ratio	Elastic modulus E_d (MPa)	Allowable pressure σ (MPa)
Soft rubber	0.1–0.2	5	25–50
Harder rubber	0.3–0.4	20–25	50–83
Slotted or perforated rubber	0.2–0.25	4–5	18–25
Spongy rubber	0.03	3	100

4.2 Structural Improvement

4.2.1 Underframe

According to the above modal analysis and dynamic response analysis of underframe, the frequencies with the largest resonance amplitude at the reference point are approximately 34 Hz, 55 Hz, and 88 Hz. The underframe structure should be improved through the following measures:

Firstly, sealing plates are installed at the front and rear ends of the three *Z*-direction beams in the middle of underframe and reinforcing ribs are added to increase the stiffness of the connection, as shown in Figures 20(a) and (d)

Secondly, the motor, electrical box, and other devices are installed at the beam and the structure should be improved to avoid excessive vibration. The arrangement way of transverse beam stiffeners for increasing the beam stiffness is shown in Figure 20(b).

Thirdly, connecting pieces should be added between *Z*-direction beams to enhance *Y*-direction stiffness and avoid torsion in the middle of underframe, as shown in Figure 20(c).

4.2.2 Frame

According to the modal analysis and dynamic response analysis of frame, the main frequencies that cause resonance are 21 Hz, 34 Hz, 49 Hz, 55 Hz, and 67 Hz. There are many partial modes at the main beam of frame and the vibration response is strong. The frame structure of the main beam should be improved through the following measures.

Firstly, longitudinal stiffeners are added at the front and rear ends of the main beam to increase *Y*-direction stiffness of frame, as shown in Figure 21(a).

Secondly, the main beam of frame is connected with the left- and right-side beams to increase *Y*- and *Z*- direction stiffness of frame, as shown in Figure 21(b).

Thirdly, a beam is added in the middle of the main beam of frame to increase *Y*-direction stiffness of frame, as shown in Figure 21(c).

4.3 Damping Vibration

Damping refers to the physical phenomenon in which the vibrating system is blocked and the energy is dissipated into other forms of energy, such as heat. When the metal plate shell coated with a high-damping material is excited to vibrate, the damping layer also vibrates.

The skin on the surface of the grinding vehicle body is a thin plate, which contains little damping, and has the high sound radiation efficiency. Therefore, the radiation noise generated by the skin vibration is mainly considered. In this section, a free damping structure is adopted and a layer of damping material is added to the skin substrate to increase structural damping and reduce vibration and noise, as shown in Figure 22.
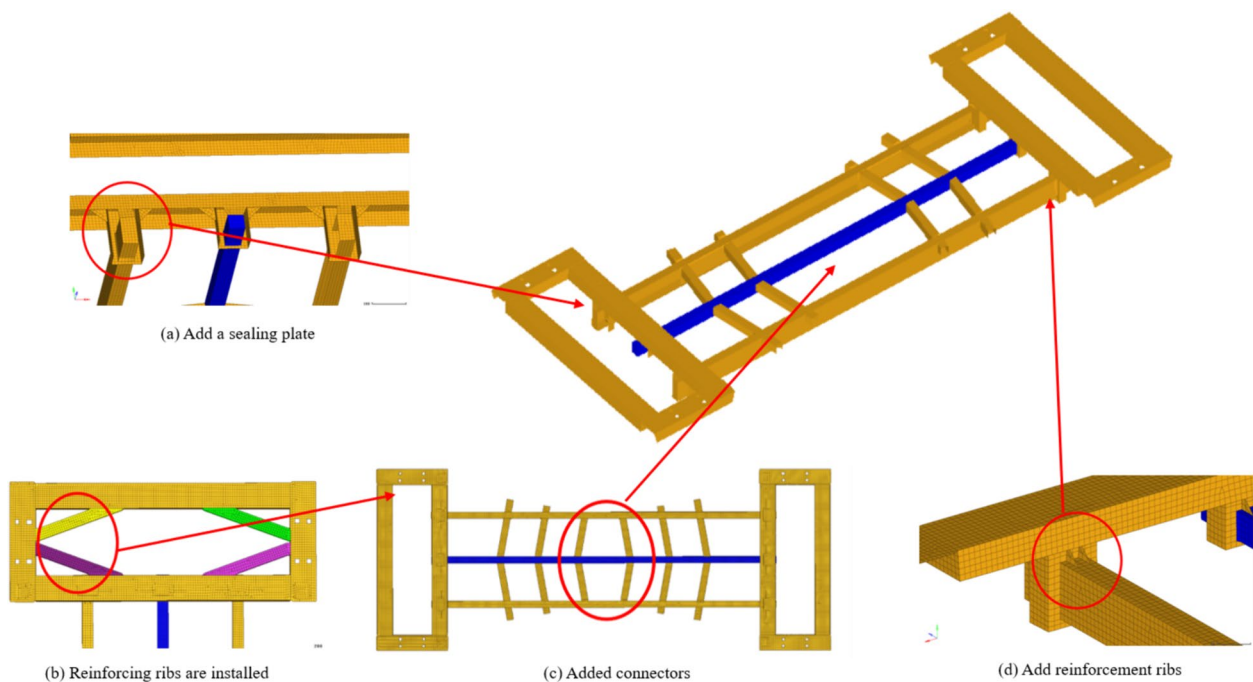

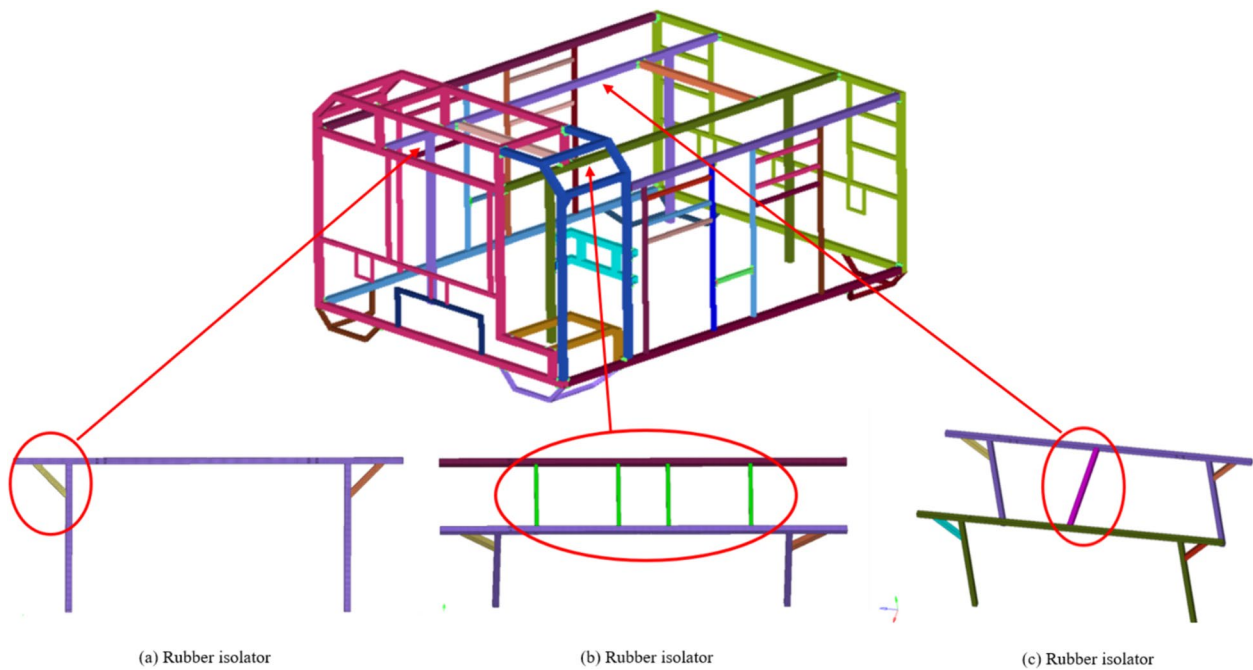**Figure 20** Schematic diagram of underframe optimization

(a) Rubber isolator   (b) Rubber isolator   (c) Rubber isolator

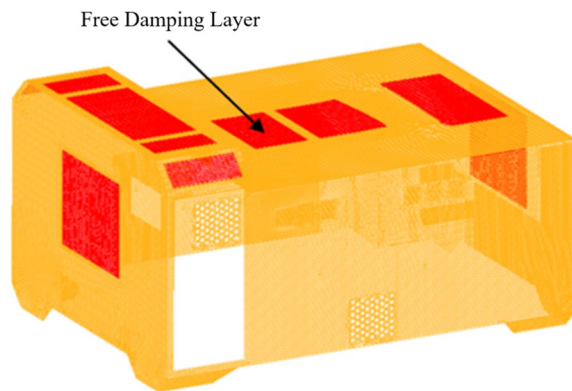**Figure 21** Schematic diagram of frame optimization

Free Damping Layer

Figure 22 Skin vibration and noise damping control scheme

According to Table 9, the damping material of free damping layer is soft rubber with the loss factor η_2 of $2 \times 10^{-1} \sim 5$ and the elastic modulus E_2 of 0.00784 GPa. The aluminum alloy skin E_1 is 70 GPa and E_2/E_1 is 1.12×10^{-4}, which meets the standard of the elastic modulus ratio. According to the standard thickness ratio H_1/H_2 of 2 to 4, the thickness of the damping material is selected as 8 mm.

4.4 Vibration Reduction Effect Analysis

The above vibration control scheme is applied in the finite element model of the whole vehicle and the dynamic response of the improved rail grinding vehicle with abrasive belt is analyzed and evaluated under non-operating and grinding operating conditions.

According to the dynamic response results of the improved model, the vibration acceleration value of each

Table 10 Effective values of vibration acceleration at reference points of each part after improvement

Directions	Front of underframe	Middle of underframe	Main beam of frame	Contact wheel	Skin upper plate	Dust collection system
X-direction	0.8930	3.8187	3.4644	10.5675	0.9422	2.3668
Y-direction	4.3417	3.1534	8.1188	3.1403	5.3548	2.4854
Z-direction	4.1509	3.7274	1.0379	12.0247	0.2868	2.3976
Average	3.1285	3.5665	4.2070	8.5775	2.1946	2.4166

reference point is extracted and RMS value of vibration acceleration of each reference point is calculated (Table 10).

Z-direction vibration acceleration of the front end of underframe under the non-operating condition is the largest among the three operating conditions, so the dynamic response under the non-operating condition is analyzed. *Z*-direction vibration acceleration of the front end of underframe is calculated to be 5.08 m/s^2 and *Y*-direction vibration acceleration of the front end of underframe is 0.93 m/s^2. The calculation results meet the limit values in GB/T 17426-1998. The results show that the vibration control effect of vehicle meets the stability requirements.

RMS value of vibration acceleration of the whole vehicle under the operating condition is calculated to be 7.00 m/s^2. Compared with the RMS value of vehicle vibration acceleration in the original model under operating conditions (15.60 m/s^2), the RMS value of the improved model is reduced by approximately 55%. The contact wheel is in the direct contact with the rail and the vibration reduction effect is not obvious. In the vibrations of other parts, only the *Y*-direction vibration of the main frame of frame exceeds the standard value in GB/T 17426-1998. However, after optimization, the vibration acceleration is significantly reduced from 11.90 m/s^2 to 8.12 m/s^2. RMS value of vibration acceleration of the upper skin plate is 2.19 m/s^2. After optimization, RMS value of the vehicle skin vibration acceleration under operating conditions is 7.34 m/s^2, which is approximately 30% of that of the original model. The results show that the vibration control scheme has an obvious vibration reduction effect.

5 Lightweight Design

In order to further explore the dynamic characteristics of the grinding vehicle, the random vibration simulation analysis is carried out. The lightweight design of grinding vehicles is conducive to transferring and transportation. The vibration control and lightweight design of the mill is carried out by changing the frame material.

5.1 Finite Element Model

To facilitate the simulation calculation of the lightweight design, the grinding vehicle model is further simplified as a small model. The whole vehicle is divided into four main parts, as shown in Table 11. Each part is simplified as a solid unit. The total weight is 1500 kg. The skin material is selected as aluminum alloy 6061 and the other parts are set as channel steel Q235. The underframe, skin, and frame structure are simulated by shell elements and the mesh size is still 10 mm. The wheelset and grinding elements are simulated by solid elements and the mesh size is 10 mm. The welding is simulated by seam

Table 11 Weight distribution table of the grinding vehicle

Structural elements	Weights (kg)	Remarks
Frame	420	
Underframe	210	
Grinding unit	80	Each
Skin	80	
Wheel	100	Per pair

elements. Bearings and bolt connections are simplified as solid elements and each assembly surface is simulated by the RBE2 element with the default damping parameter of 0.01.

The new finite element analysis model is established in Hypermesh with a total of 930000 nodes and 830000 elements, as shown in Figure 23.

The skin is selected as 1 mm thick aluminum alloy and the optimization effect is not obvious. In the optimization of the grinding unit, the grinding quality may be affected. The wheelset optimization involves material replacement, process optimization, and a new design and is cumbersome. In the frame optimization, the weight can be reduced by 20%–30% only by changing the material.

According to the above analysis in Section 3, the original grinding vehicle vibrates violently. The method of replacing the frame material with 7075 aluminum alloy and LA43M magnesium alloy is adopted for the non-optimized grinder vehicle to achieve vibration reduction and lightweight design. The three selected materials are shown in Table 12.

5.2 Random Vibration

The rail has random irregularities in all directions and the random occurrence of track diseases also follows a normal distribution [42]. For example, the wave grinding wavelength is approximately 50 to 150 mm. The probability of rail corrugation at the wavelengths of 50 and 150 mm is low and the probability at the wavelength of 100 mm is high. In the transient dynamics simulation, only the excitations of several fixed frequencies can be input and transient dynamics simulation has certain limitations in the field of rail grinding. Therefore, random vibration simulation is performed to simulate the vibration caused by rail defects.

Track disease data simulated by software are random data, but collected actual disease data are not necessarily representative data. Based on the comprehensive consideration, the power spectral density of the horizontal irregularity of the American AAR6 track, which is highly recognized internationally, is selected as the input condition of the random vibration simulation in Ansys. The

action position of the power spectral density of the horizontal irregularity is on the wheelset and contact wheel.

According to the simulation conditions of the above model and random vibration analysis results, the stress distribution of the Q235 steel frame grinding vehicle can be obtained (Figure 24 and Table 13). The vibration on the frame is mainly distributed in the connection position between underframe and electrical rack.

According to Miner's linear fatigue cumulative damage theory, when a material is subjected to cyclic stress
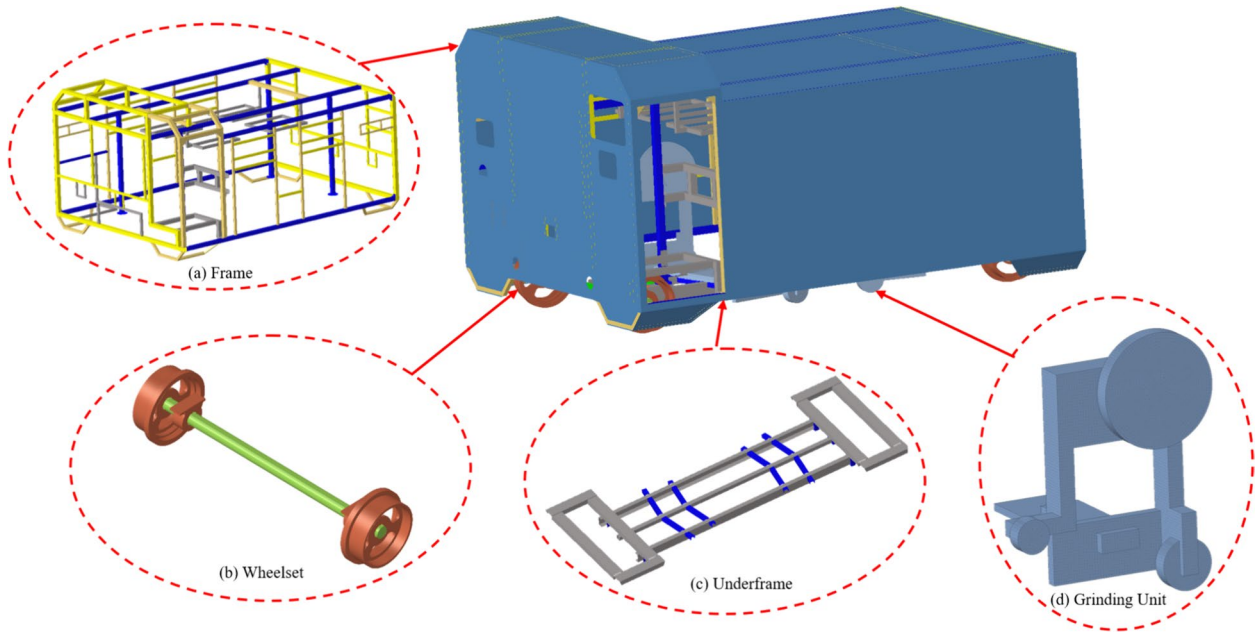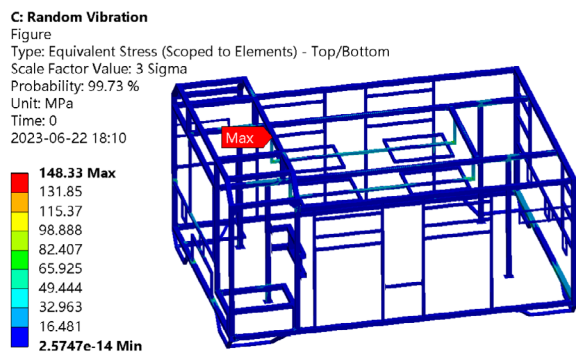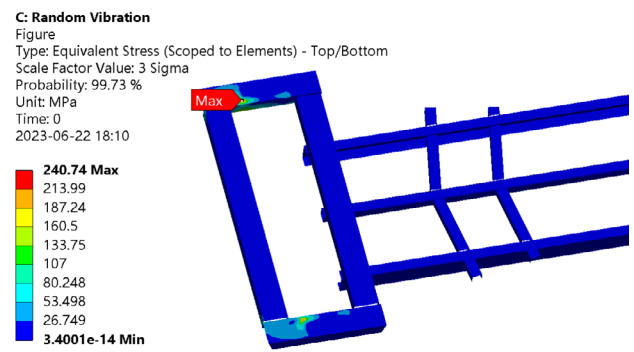

Figure 23 Finite element model of rail grinding vehicle with abrasive belt

Table 12 Details of selected frame materials

Materials	Density (g/cm³)	Elastic modulus (GPa)	Poisson's ratio	Yield strength (MPa)
Steel Q235	7.85	210	0.30	235
Aluminum alloy 7075	2.85	71	0.33	477
Magnesium alloy LA43M	1.78	45	0.35	125

(a) Q235 stress distribution

(b) Q235 maximum stress

Figure 24 Schematic diagram of vibration distribution

Table 13 Maximum equivalent stress results under 3σ random vibration (MPa)

Materials	Vehicles	Frames	Underframe	Skin	Grinding unit	Wheel
Steel Q235	240.7	148.3	240.7	30.9	1.5	13.6
Aluminum alloy 7075	166.0	84.0	166.0	21.5	0.7	5.3
Magnesium alloy LA43M	160.0	42.4	160.0	26.7	0.7	4.9

higher than its fatigue limit, each stress cycle causes a certain damage to the material and this damage can be accumulated [43]. Destruction occurs when the accumulated damage exceeds a critical value. According to the three-interval method based on the Gaussian distribution and Miner's linear cumulative damage law proposed by Steinberg [44, 45], the stress distribution can be divided into three main intervals: 1σ, 2σ, and 3σ. The distribution probabilities corresponding to 1σ, 2σ, and 3σ are respectively 68.3%, 27.1%, and 4.33% and the total distribution probability of three intervals is 99.73%. The distribution probability of the rest interval can be ignored.

According to Miner's linear fatigue cumulative damage theory, a frequency domain stress lower than the material's yield limit generally does not cause a damage to the material. According to the simulation results, the most severe vibration occurs at the connection between the chassis and the wheelset. The stress at the position of strip exceeds the yield limit of the material and can not satisfy the 3σ safety condition.

5.3 Vibration Control

The main load of frame is the four power supplies on the electrical rack and the strength of aluminum alloy or magnesium alloy can meet the requirements for static strength. After the frame material is replaced with 7075 aluminum alloy and LA43M magnesium alloy, the random vibration analysis of the above conditions is carried out. The vibration distribution of the grinding vehicle basically remains unchanged after changing different frame materials. The analysis results are listed in Table 13. Figure 25 shows the stress distribution diagram of the grinding vehicle after changing frame material to aluminum or magnesium alloy.

The simulation results show that when aluminum alloy 7075 and magnesium alloy LA43M are used, the stress of frame and other structures can be reduced and the yield failure does not occur in various parts of the whole grinding vehicle. In addition, the weight of vehicle body can be reduced. The lightweight results are provided in Table 14.

As the elastic modulus of frame material decreases, the stiffness of frame decreases and the response of grinding vehicle to vibration becomes insensitive. Therefore, the stress generated by the vibration also decreases,

displaying a certain vibration reduction effect. In addition, the elastic modulus of frame is reduced and the rigidity of the whole vehicle is reduced, displaying the similar effect to the addition of damping components. The vibrations of all components affect each other and the damping effect is gradually weakened. After the vibration is transmitted from wheel to underframe, frame, and skin, the vibration of skin and frame also affects the underframe and wheelset. Therefore, compared with channel steel Q235, the other materials of frame can be used as a vibration damping element to reduce the underframe vibration caused by frame and skin. In this way, the vibration response stress of underframe is also reduced.

In summary, as the elastic modulus of frame decreases, the sensitivity of frame itself to vibration decreases. With the reduction of the elastic modulus of frame, the stiffness of the whole vehicle is reduced so as to decrease the vibration response of other structures. In the selection of the materials of support structures under vibration, the materials with qualified static strength, lower density, and smaller elastic modulus are recommended because these materials can reduce the overall vibration and realize the lightweight design.

6 Conclusions

In this paper, the vibration control of the rail grinding vehicle with abrasive belt is explored based on dynamic characteristics through structural optimization and lightweight design. The conclusions are drawn below:

(1) The transient response of the vehicle caused by the combined action of multiple excitations under non-operating conditions and operating conditions is analyzed. The RMS value of the maximum vibration acceleration of the whole vehicle is 3.20 m/s^2 under the non-operating condition and 15.60 m/s^2 under the operating condition. The acceleration in the partial directions of the reference points of the grinding vehicle exceeds the limit in GB/T 17426-1998 standard.

(2) A random vibration simulation analysis of the grinding vehicle with three frame materials under the excitation of the six-level track spectrum hori-
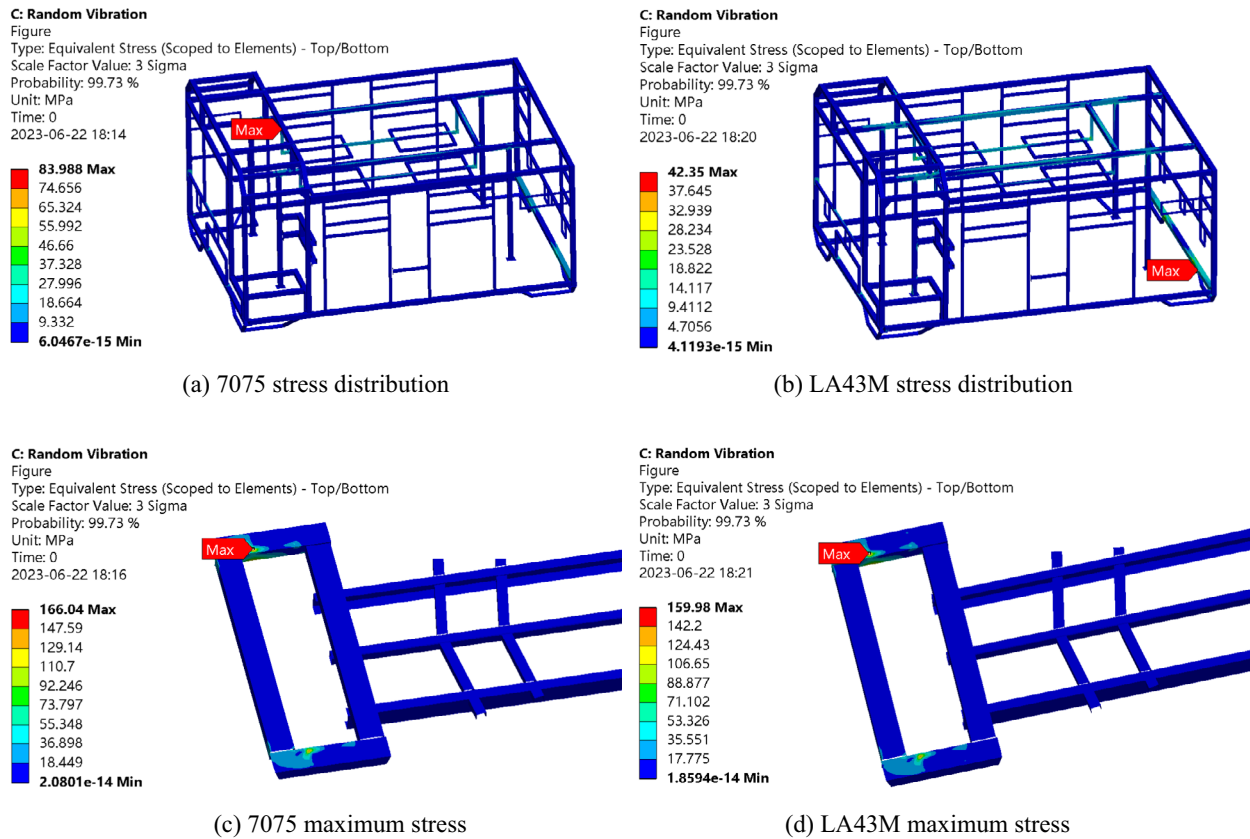
(a) 7075 stress distribution

(b) LA43M stress distribution

(c) 7075 maximum stress

(d) LA43M maximum stress

Figure 25 Schematic diagram of the vibration distribution

Table 14 Lightweight design results

Materials	Frame weight (kg)	Frame stress (MPa)	Strength (MPa)	Weight loss rate (%)	Safety
Steel Q235	420	148.3	235	–	2σ
Aluminum alloy 7075	152	84.0	455	17.9	3σ
Magnesium alloy LA43M	95.2	42.4	125	21.7	3σ

Note: Weight reduction rate = (original frame mass - frame mass)/vehicle mass

zontal irregularity in the United States is carried out. The analysis results show that the Q235 steel frame does not satisfy the safety conditions of 3σ.

(3) By optimizing the structure of the grinding vehicle in three ways, the average vibration acceleration of the whole vehicle is decreased from 15.60 m/s^2 to 7.00 m/s^2 and the percentage decrease is about 55.1%. By changing frame material, the maximum vibration stress of the vehicle is decreased from 240.7 MPa to 160.0 MPa. The weight of the grinding vehicle is decreased by from 1500 kg to 1175 kg and the percentage decrease is about 21.7%. Therefore, the vibration control of the grinding vehicle can be realized by optimizing the structure accord-

ing to the modal analysis results and replacing the materials with enough strength and lower stiffness.

Authors' Contributions
WF was in charge of the whole trial; SZ wrote the manuscript; ZW and YL directed the writing; JY completed the simulation research on the dynamic characteristics and vibration control of transient dynamics. SZ completed the simulation research on the dynamic characteristics and vibration control of random vibration. All authors have read and approved the final manuscript.

Availability of Data and Materials
The datasets supporting the conclusions of this article are included in the article.

Declarations

Competing Interests
The authors declare no competing financial interests.

References

[1]   W G Fan, W X Wang, J D Wang, et al. Microscopic contact pressure and material removal modeling in rail grinding using abrasive belt. *Proceedings of the Institution of Mechanical Engineers, Part B: Journal of Engineering Manufacture*, 2021, 235(1-2): 3-12.

[2]   W G Fan, Y M Liu, X Y Song, et al. Influencing mechanism of rubber wheel on contact pressure and metal removal in corrugated rail grinding by abrasive belt. *Journal of Manufacturing Science and Engineering: Transactions of the ASME*, 2018, 140(12): 124501.

[3]   W G Fan, C H Wu, Z W Wu, et al. Static contact mechanism between serrated contact wheel and rail in rail grinding with abrasive belt. *Journal of Manufacturing Processes*, 2022, 84: 1229-1245.

[4]   Z W Wu, W G Fan, C Qian, et al. Contact mechanism of rail grinding with open-structured abrasive belt based on pressure grinding plate. *Chinese Journal of Mechanical Engineering*, 2023, 36: 42.

[5]   J N Yu. *Research on dynamic simulation analysis and vibration control of rail grinding vehicle by abrasive belt*. Beijing: Beijing Jiaotong University, 2021. (in Chinese)

[6]   A A Rashid, R Imran, Z U Arif. Finite element simulation technique for evaluation of opening stresses under high plasticity. *Journal of Manufacturing Science and Engineering: Transactions of the ASME*, 2021, 143(12): 1-7.

[7]   S H Zhou, G Q Song, M N Sun, et al. Nonlinear dynamic analysis of a quarter vehicle system with external periodic excitation. *International Journal of Non-Linear Mechanics*, 2016, 84: 82-93.

[8]   A Hilleborg. A study of dynamic influences of moving loads on girders. *IABSE, Third Congress*, 1948: 661-667.

[9]   A A Ahmed, J Santhosh, F W Aldbea. Vehicle dynamics modeling and simulation with control using single track model. *2020 IEEE International Women in Engineering (WIE) Conference on Electrical and Computer Engineering (WIECON-ECE)*, India, 2020: 1-4.

[10] G B Luo, J Zeng, Q S Wang. Identifying the relationship between suspension parameters of underframe equipment and carbody modal frequency. *Journal of Modern Transportation*, 2014, 22(4): 206-213.

[11] T Gillespie. Fundamentals of vehicle dynamics. *SAE International*, 2021.

[12] Z Q Yi, J Xie, S P Li, et al. Elastic dynamic analysis and optimization design of the turntable mechanism for rail grinding. *Journal of Railway Science and Engineering*, 2018, 15(6): 1551-1558. (in Chinese)

[13] J N Costa, P Antunes, H Magalhães, et al. A finite element methodology to model flexible tracks with arbitrary geometry for railway dynamics applications. *Computers & Structures*, 2021, 254: 106519.

[14] C Y Du. *Research on dynamic performance of rail grinding train*. Chengdu: Southwest Jiaotong University, 2018. (in Chinese)

[15] P Shen, H Q Cao, Y L Qiao. Research on dynamic performance of rail grinding vehicle. *Western Leather*, 2019, 41(8): 88-89. (in Chinese)

[16] C Y Zhao C, J Y Li, W G Fan, et al. Experimental and simulation research on residual stress for abrasive belt rail grinding. *The International Journal of Advanced Manufacturing Technology*, 2020, 109(1): 129-142.

[17] Z Q Wang, Z Y Lei. Dynamic characteristics of a wheelset–track system under corrugation excitations in the metro operation process. *Transactions of the Canadian Society for Mechanical Engineering*, 2020, 45(3): 411-420.

[18] S Y Zhang, J Z Jiang, S A Neild. Passive vibration control: A structure-immittance approach. *Proc. Math. Phys. Eng. Sci.*, 2017, 473(2201): 20170011.

[19] P S Balaji, K Karthik SelvaKumar. Applications of nonlinearity in passive vibration control: A review. *Journal of Vibration Engineering & Technologies*, 2021, 9(2): 183-213.

[20] Z X Zong. Study on vibration reduction method of passive vibration absorber for urban rail vehicle body. *Railway Locomotive & Car*, 2021, 41(1): 123-128. (in Chinese)

[21] İ Eski, Ş Yildirim. Vibration control of vehicle active suspension system using a new robust neural network control system. *Simulation Modelling Practice and Theory*, 2009, 17(5): 778-793.

[22] H Liu, X Zhang, Y Chen, et al. Active damping of driveline vibration in power-split hybrid vehicles based on model reference control. *Control Engineering Practice*, 2019, 91: 104085.

[23] G I Y Mustafa, H P Wang, Y Tian. Vibration control of an active vehicle suspension systems using optimized model-free fuzzy logic controller based on time delay estimation. *Advances in Engineering Software*, 2019, 127: 141-149.

[24] Q Cai, S Zhu. The nexus between vibration-based energy harvesting and structural vibration control: A comprehensive review. *Renewable and Sustainable Energy Reviews*, 2022, 155: 111920.

[25] C Zhang, H Kordestani, M Shadabfar. A combined review of vibration control strategies for high-speed trains and railway infrastructures: Challenges and solutions. *Journal of Low Frequency Noise, Vibration and Active Control*, 2023, 42(1): 272-291.

[26] C H Huang. *Research on vibration reduction technology of high speed vehicles*. Chengdu: Southwest Jiaotong University, 2012. (in Chinese)

[27] G W Jang, M S Yoon, J H Park. Lightweight flatbed trailer design by using topology and thickness optimization. *Structural and Multidisciplinary Optimization*, 2010, 41(2): 295-307.

[28] J Plocher, A Panesar. Review on design and structural optimisation in additive manufacturing: Towards next-generation lightweight structures. *Materials & Design*, 2019, 183: 108164.

[29] B S Yıldız, A R Yıldız, N Pholdee, et al. The Henry gas solubility optimization algorithm for optimum structural design of automobile brake components. *Materials Testing*, 2020, 62(3): 261-264.

[30] S H Liu, Y B Du, M Lin. Study on lightweight structural optimization design system for gantry machine tool. *Concurrent Engineering*, 2019, 27(2): 170-185.

[31] K U Bletzinger, E Ramm. Structural optimization and form finding of light weight structures. *Computers & Structures*, 2001, 79(22): 2053-2062.

[32] S Rosenthal, F Maaß, M Kamaliev, et al. Lightweight in automotive components by forming technology. *Automotive Innovation*, 2020, 3(3): 195-209.

[33] F Czerwinski. Current trends in automotive lightweighting strategies and materials. *Materials*, 2021, 14(21): 6631.

[34] J T J Burd, E A Moore, H Ezzat, et al. Improvements in electric vehicle battery technology influence vehicle lightweighting and material substitution decisions. *Applied Energy*, 2021, 283: 116269.

[35] P K Mallick. *Materials, design and manufacturing for lightweight vehicles*. Woodhead Publishing, 2020.

[36] Y Q Yuan. *Study on the mechanism and influence of the wheel out-of-round of high speed train*. Beijing: Beijing Jiaotong University, 2016. (in Chinese)

[37] L S Tian. *MSC nastran dynamic analysis guide*. China Water & Power Press, 2012: 7-10. (in Chinese)

[38] Z W Liu, J X Liu, J F Cai. Vibration response analysis of heavy haul locomotives excited by rail corrugation. *Noise and Vibration Control*, 2020, 40(5): 119-125. (in Chinese)

[39] National Bureau of Standards. *Dynamic performance evaluation and test method for particular class vehicles and tracked machine*. Beijing: China Railway Publishing House, 1998: 1-5. (in Chinese)

[40] M P Sheng, M Q Wang, J G Ma. *Basics of noise and vibration control technology*. Beijing: Science Press, 2001. (in Chinese)

[41] E H Zhang, J Y Yin, S R Xing. *Noise and vibration control*. Metallurgical Industry Press, 2012: 52-89. (in Chinese)

[42] P X Huang, F C Lan, J Q Chen. The structural response analysis of EV battery pack under random vibration and impact conditions. *Automotive Engineering,* 2017, 39(9): 1087-1093,1099. (in Chinese)

[43] Y M Bai, E J Qiu, H J Wang. Random vibration fatigue life analysis and optimization design of connector based on ANSYS. *Journal of Ordnance Equipment Engineering,* 2019, 40(11): 178-182. (in Chinese)

[44] Q Peng, G H Wang. Fatigue life prediction for aero-engine turbine disk based on the finite element analysis. *Journal of Ordnance Equipment Engineering,* 2018, 39(8): 176-178. (in Chinese)

[45] S Feng, Y P Cheng, L Y Zhao, et al. Linear fatigue damage cumulation theory. *Journal of Harbin Institute of Technology,* 2003, 35(5): 608-610. (in Chinese)

Wengang Fan   born in 1985, is currently an associate professor at *Beijing Jiaotong University, China*. He received his PhD degree from *Beijing Jiaotong University, China*, in 2012. His main research direction is rail grinding technology and equipment, digital manufacturing technology and equipment.

Shuai Zhang   born in 1998, is currently a master candidate at *Key Laboratory of Vehicle Advanced Manufacturing, Measuring and Control Technology, Ministry of Education, Beijing Jiaotong University, China*. He received his bachelor degree from *Beijing Jiaotong University, China*, in 2021.

Zhiwei Wu   born in 1994, is currently a PhD candidate at *Key Laboratory of Vehicle Advanced Manufacturing, Measuring and Control Technology, Ministry of Education, Beijing Jiaotong University, China*. He received his master degree from *North China University of Technology, China*, in 2020.

Yi Liu   born in 1998, is currently a master candidate at *Key Laboratory of Vehicle Advanced Manufacturing, Measuring and Control Technology, Ministry of Education, Beijing Jiaotong University, China*. She received her bachelor degree from *China University of Geosciences Beijing, China*, in 2020.

Jiangnan Yu   born in 1997, is currently an engineer at *China Railway Materials Operation and Maintenance Technology Co., Ltd., China*. He received his master degree from *Beijing Jiaotong University, China*, in 2021.